# A Flux-Flux Analysis of Spectral Variability in Markarian 335

by

Hannah Ehler

A THESIS SUBMITTED IN PARTIAL FULFILMENT OF
THE REQUIREMENTS FOR THE DEGREE OF

BACHELOR OF SCIENCE

in

Honours Astrophysics

(Department of Astronomy and Physics, Dr. Luigi Gallo supervising faculty)

. . . . . . . . . . . . . . . . . . . . . . . . . . . . . . . . . . . . . . . . . . . . . . . . . . . . . . . . . .

. . . . . . . . . . . . . . . . . . . . . . . . . . . . . . . . . . . . . . . . . . . . . . . . . . . . . . . . . .

. . . . . . . . . . . . . . . . . . . . . . . . . . . . . . . . . . . . . . . . . . . . . . . . . . . . . . . . . .

. . . . . . . . . . . . . . . . . . . . . . . . . . . . . . . . . . . . . . . . . . . . . . . . . . . . . . . . . .

. . . . . . . . . . . . . . . . . . . . . . . . . . . . . . . . . . . . . . . . . . . . . . . . . . . . . . . . . .

SAINT MARY'S UNIVERSITY

April 18, 2017

© Hannah Ehler, 2017

# ACKNOWLEDGMENTS

Many thanks to thank my supervisor Dr. Luigi Gallo for his patience and guidance
over the past two years. I would also like to thank the SMASHERS group for their
input and assistance, Dr. Dan Wilkins, Kirsten Bonson, and Adam Gonzalez.
Thanks be to the Computer Whisperer, Tiffany Fields, for her succor in matters of
programming.

# Abstract

A Flux-Flux Analysis of Spectral Variability in Markarian 335

by *Hannah Ehler*

submitted on April 18, 2017:

Markarian 335, a Narrow-Line Seyfert 1 Galaxy, has been one the brightest X-ray sources in the sky until 2007 when its flux dropped to 1/10th of its previous value. Despite this dramatic decrease, Mrk 335 still remains one of the brighter AGN in the X-ray, and is a highly variable source. Flux-Flux Plots, a model-independent technique, were utilized to determine the mode of spectral variability in this AGN. Flux-Flux Plots were created using X-ray data from *XMM-Newton* to examine spectral variability on short timescales (e.g. $\leq 1$ day). Binning up the Flux-Flux Plots produced different results depending on the dimension the data were binned by, indicating that there is more than one varying component present. Simple models with only varying component fit to the Flux-Flux plots were poor and nearly indistinguishable, further indicating that the spectral variability in Mrk 335 is more complex than can be described by a single variable component. A Time-Resolved Flux-Flux analysis of the observation XMM-Int1 revealed a change in variability at $\sim 70$ ks, which corroborates previous studies. It seems that the spectral variability in Mrk 335 is likely the result of the variation of multiple parameters simultaneously.

# Contents

# List of Figures

# List of Tables

# Chapter 1

# INTRODUCTION

## 1.1 ACTIVE GALACTIC NUCLEI

### 1.1.1 UNIFIED MODEL

Supermassive black holes reside at the centre of most, if not all, galaxies. These black holes can have masses on the order of millions of solar masses. A small fraction of these black holes accrete material and emit energy; these are considered "active" and so called Active Galactic Nuclei (AGN). These objects emit radiation at all wavelengths across the electromagnetic spectrum and are extremely bright, outshining their host galaxy. The spectrum of an AGN typically peaks in the ultraviolet (Gallo, 2011), though AGN emit at all wavelengths.

The unified model suggests that all types of AGN are fundamentally the same, powered by the same central engine (Carrol and Ostlie, 2007). The basic model of an Active Galactic Nuclei is shown in Figure 1.1. It features a supermassive black hole at the centre of a galaxy, surrounded by an accretion disc. It is the accretion of material from this disc onto the black hole that powers the emission of the source. AGN are very efficient at generating radiation through the accretion process, with an efficiency up to 40% (Gallo, 2011). Exterior to the accretion disc resides a dusty torus, marking the outer boundary of the broad line region.
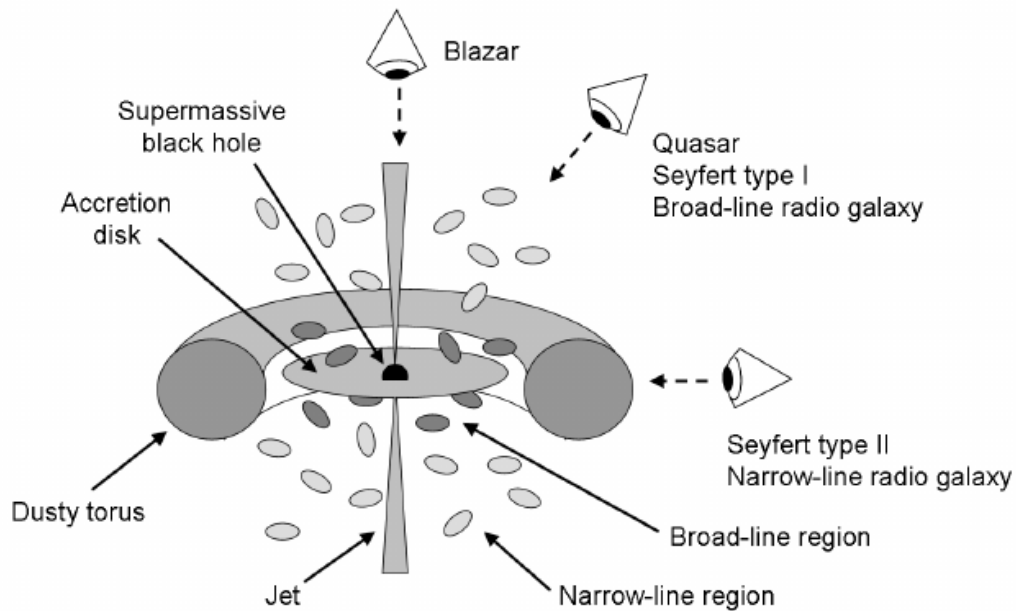
Figure 1.1: Unified model of AGN, from Zackrisson (2005).

The broad-line region is the region close to the black hole that is affected by the black hole's gravity, causing emission lines in this region to be Doppler broadened. The electron number density is between $10^{15}$ and $10^{18}$ m$^{-3}$ (Carrol and Ostlie, 2007). This number density is too large to permit forbidden transitions, so forbidden spectral lines are not observed in the broad line region (Carrol and Ostlie, 2007). This region is inhomogeneous and clumpy, containing partially ionised, optically thick clouds (Carrol and Ostlie, 2007). These clouds occupy only 1% of the broad-line region's volume and likely exhibit a flattened distribution (Carrol and Ostlie, 2007). The dusty torus can obscure the broad-line region depending on the orientation of the AGN relative to our line of sight.

Outside the torus lies the narrow-line region. This region is not influenced by gravitational effects of the black hole and so the emission lines produced in this

region are narrow. The number density of electrons in the narrow-line region is on the order of $10^{10}$ m$^{-3}$ and so forbidden transitions are permitted (Carrol and Ostlie, 2007). The narrow-line region contains clumpy clouds like the broad line region, but unlike the broad-line region, these clouds are likely spherical in distribution (Carrol and Ostlie, 2007).

Our line of sight to the black hole through the obscuring torus will determine what is observed and how the AGN is classified. Seyfert galaxies are spiral galaxies with strong emission lines that are further classified as type I or II (or somewhere in-between) based on properties of the emission lines in their spectra. Seyfert I galaxies are AGN of which we have a clear line of sight to the broad-line region, and so their spectra contain both broad and narrow lines. Seyfert II spectra bear only narrow lines, as the torus obscures the broad-line region from our line of sight to these galaxies, and we observe only the narrow-line region.

Some AGN have jets, containing ionised gas moving at relativistic velocities (Ryden and Peterson, 2010). These jets can emit at X-ray, visible, and radio wavelengths (Ryden and Peterson, 2010) and can extend to scales larger than the host galaxy (Gallo, 2011). An AGN that is viewed by a line of sight of parallel to the jet is classified as a quasar. Quasars have very high luminosities and are further subdivided based on their radio emission.

## 1.1.2 X-RAY REGION

The AGN central engine is an accretion disc around a supermassive black hole at the core of an active galaxy. It is the accretion of material from this disc onto the black hole that produces emission. X-ray emission is seen to vary over timescales as brief as hours (see Section 1.2). Because variations cannot occur faster than it takes light to travel across the region, rapid variability indicates that the X-rays originate from regions closest to the black hole (Gallo, 2011). The X-ray emitting region of a supermassive black hole of mass $10^7$ M$_\odot$ is approximately the size of our solar system (Gallo, 2011). We are unable to resolve the X-ray emitting regions of AGN and so must rely on spectral and timing analysis to further our understanding of the regions and processes therein (Gallo, 2011).
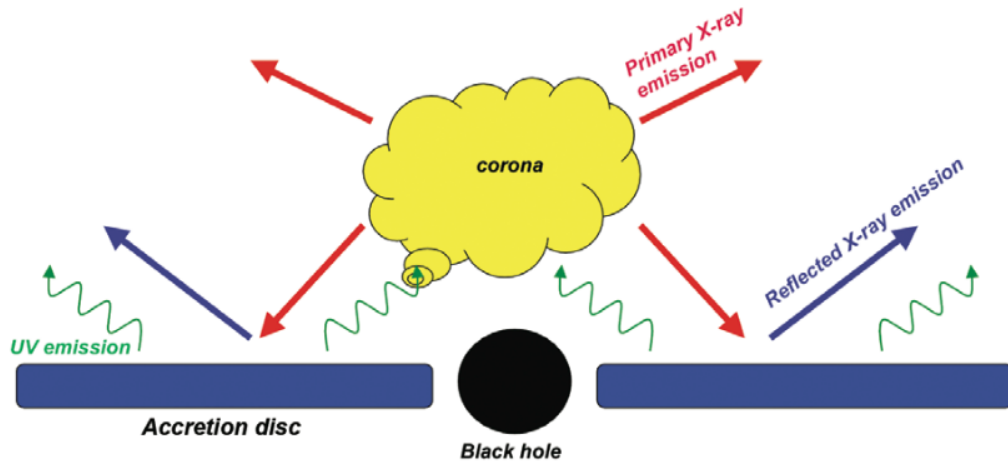


Figure 1.2: Inner region of AGN, from Gallo (2011).

The geometry of the X-ray emitting region is depicted in Figure 1.2. This region consists of two components: a primary emitter and an accretion disc.

The primary emitter is the corona: an extended atmosphere of hot electrons that resides above the black hole (Gallo, 2011). These electrons are likely dredged up from the accretion disc during the accretion process and deposited in the corona via magnetic reconnection (Galeev et al., 1979). When thermal ultraviolet photons emitted from the accretion disc encounter the corona, they are up-scattered to higher energies and re-emitted as X-rays in a process called Comptonization (Wilkins and Gallo, 2015b). This X-ray emission from the corona constitutes the primary emission and is represented by a power-law in the spectrum (see Figure 1.3). This power-law has a high-energy cut-off which indicates the temperature of the corona (Gallo, 2011). The geometry of the corona remains unknown; models including point source and extended geometries have been suggested, as well as evolving geometries (Wilkins, 2016; Gonzalez et al., in print).

The primary emission is emitted isotropically and so some of these X-rays encounter the accretion disc. The accretion disc, being cooler and optically thick, will back scatter some of the primary emission, comprising the reflected emission. As the material in the accretion disc is struck by the primary emission, the atoms become ionized. Photons are then released as higher-level electrons transition to lower-levels in a process called fluorescence. This produces emission lines in the reflected spectrum which can provide insight as to the ionisation and Comptonization of the inner accretion disc (Gallo, 2011). Additionally, the reflected spectrum can reveal dynamics of the innermost region as processes become imprinted on the spectrum (Gallo, 2011). Intrinsically narrow emission lines become broadened and shifted due to effects of the black hole environment. Doppler broadening occurs as a result of disc rotation

and results in a double-peaked line profile (Gallo, 2011). Special relativistic effects produce an asymmetric profile as light toward the observer appears beamed (Gallo, 2011). General relativistic effects further redshift the emission line as photons lose energy escaping from the gravitational potential well of the black hole (Gallo, 2011). The observed reflection spectrum exhibits all these effects and is thus "blurred".

The X-ray spectrum that is observed from an AGN is a combination of the primary emission and reflected emission, as depicted in Figure 1.3.
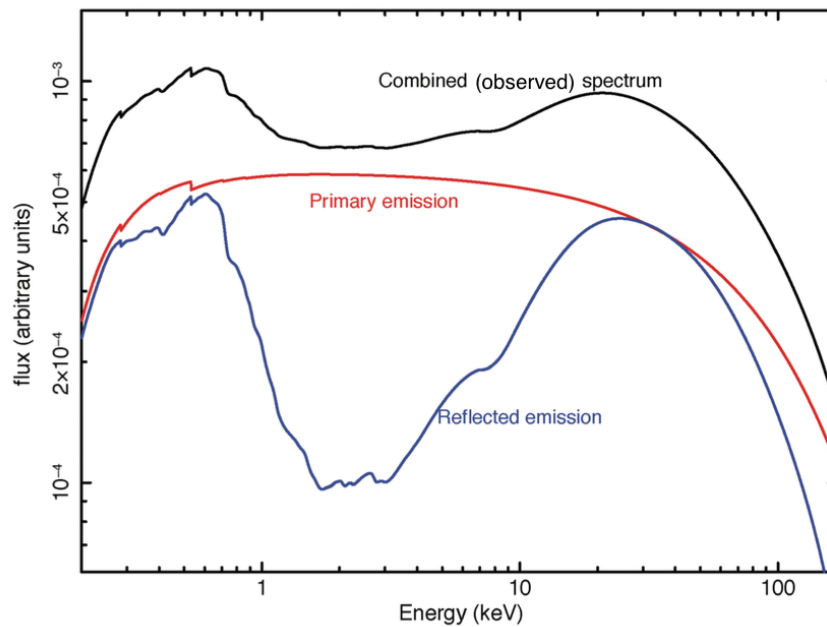
Figure 1.3: Observed spectrum of an AGN and its primary and reflected components, from Gallo (2011).

## 1.2 AGN VARIABILITY

AGN vary in brightness on all observable time scales and at all wavelengths due the accretion of matter from the accretion disc onto the black hole. The variation of the two spectral constituents, the primary emitter and the accretion disc, are what give rise to spectral variability in an AGN. However, it is far more complex than simply a variation of two components. Variation of these components can be correlated, anti-correlated, or uncorrelated. Additionally a range of parameters could contribute to the variability, including ionisation, photon index, and relative brightness of each component.

Short timescale variability is seen in the X-ray part of the spectrum, so by studying the X-ray spectra of AGN it is possible to better understand the workings and geometry of the region closest to the black hole. Over the course of mere hours, X-ray flux in AGN can vary by factors of 2-3 and sources can transition between high and low flux states (Wilkins, 2016).
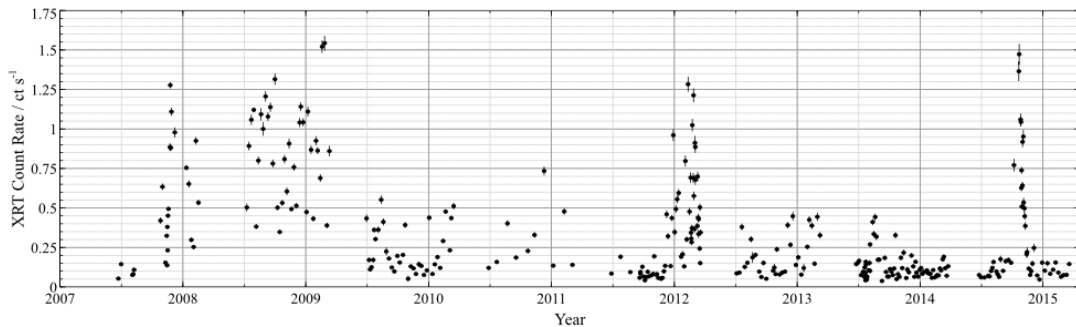


Figure 1.4: Long-term X-ray light curve of Markarian 335 exhibiting long timescale variability, from Wilkins (2016).

Additionally, long timescale variability occurs over the course of years, as depicted by the light curve of Markarian 335 in Figure 1.4. This figure reveals that Mrk 335

can vary by a factor of 15 on a yearly timescale.

Understanding the nature of AGN variability is paramount to understanding the physics and mechanisms of the innermost black hole region, especially the central engine.

## 1.3 FLUX-FLUX PLOTS

The technique employed to examine the short-term X-ray variability of Markarian 335 (Mrk 335) is the Flux-Flux Plot (FFP). This method was utilised by Taylor et al. (2003) to characterise a variety of AGN. It is a model-independent technique used to distinguish between modes of spectral variability. It plots the light curves in two energy bands against each other to see the correlation between the bands. The relationship between the bands can indicate the mode of variability. There are three simple modes of variability that can be identified from a Flux-Flux Plot. These are characterized by linear, power-law, and power-law plus constant fits to a FFP.

A linear FFP indicates that one component is changing in brightness, while maintaining constant spectral shape. This may be relative to a constant reflected component, denoted by a positive offset on the linear fit. The linear fit is given by the following:

$$y = mx + b \tag{1.1}$$

where $y$ and $x$ indicate the flux in given bands of the Flux-Flux Plot. A power-law fit to a FFP implies a spectrum that pivots about some energy. Such a fit may or may not include a constant component. The power-law fit is given by:

$$y = kx^a \tag{1.2}$$

while the power-law plus constant is:

$$y = \alpha x^{\beta} + c \tag{1.3}$$

The spectra produced by these three simple modes of variability are depicted in Figure 1.5.



(a) Linear      (b) Power-law      (c) Power-law + constant
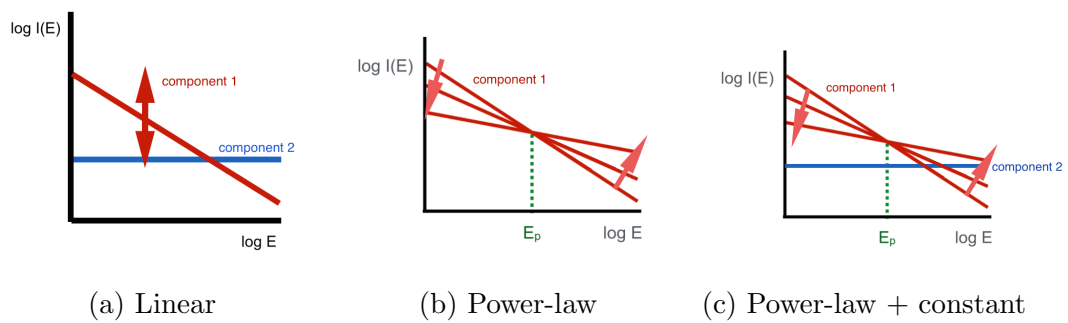
Figure 1.5: Spectra produced by different modes of variability identifiable by Flux-Flux Plots.

Modes of short-term spectral variability can be determined by making these simple fits to Flux-Flux Plots constructed from X-ray data.

## 1.4 MARKARIAN 335

Markarian 335 is Narrow-Line Seyfert 1 galaxy with a redshift of z = 0.026. At the centre of this galaxy resides an active supermassive black hole of mass $2.6 \times 10^7$ $M_\odot$ (Grier et al., 2012). Historically Mrk 335 has been one of the brightest X-ray sources in the sky, as early observations found the object in a high flux state. In 2007, observations of Mrk 335 revealed a decrease in flux by a factor of 10 from previous observations (Grupe et al., 2007). Recent observations have found the AGN in both intermediate and low flux states. The object exhibits extreme variability on all observable timescales, from hours to years, making it an ideal candidate for study. Additionally, the relatively low redshift of Mrk 335 provides adequate count rates of the source even in low flux states (Wilkins and Gallo, 2015a). Previous work on Mrk 335 has found that the X-ray spectra are described and dominated by relativistically blurred reflection (Gallo et al., 2013).

This works examines the nature of the short-term X-ray variability in Markarian 335. The model-independent Flux-Flux Plot technique is employed to determine the driver of variability for each epoch. Understanding the mode of variability can bring to light changes in the corona and accretion disc, increasing our understanding of the mechanics needed to power the most luminous sources in the Universe.

# Chapter 2

# OBSERVATIONS & DATA REDUCTION

## 2.1   *XMM-Newton*

The X-Ray Multi-Mirror Newton Observatory (*XMM-Newton*) was launched in 1999 by the European Space Agency to study cosmic X-rays. *XMM-Newton* has large collecting area telescopes that enable the collection of more photons than most X-ray observatories. The satellite is in a highly elliptical 48-hour orbit around Earth (Jansen et al., 2001).

Each of the X-ray telescopes on-board *XMM-Newton* consist of 58 nested mirrors of the Wolter I design covered in a reflective gold coating (Jansen et al., 2001). The diameter of the outermost mirror is 70 cm and the diameter of the innermost mirror is 30.6 cm, while the grazing angles of these mirrors are 42' and 17', respectively (Jansen et al., 2001). The telescopes have a focal length of 7.5 m and an effective area of 1500 cm$^2$ at 1.5 keV. (Jansen et al., 2001). The optics of *XMM-Newton* are calibrated to cover a spectral range of 0.15 - 10 keV (or 83 - 1 Å).

## 2.1.1 EPIC PN

A pn CCD detector is one of the cameras on the European Photon Imaging Camera (EPIC) and is the camera used in this work. It has high detection efficiency, low noise level, and ultrafast readout (Strüder et al., 2001). The pn consists of 12 CCD chips arranged into four quadrants containing 3 CCDs each. Each CCD chip is 3 cm × 1 cm, creating a total collecting area of 36 cm$^2$.

Table 2.1: Imaging modes of the EPIC-pn detector, from Strüder et al. (2001).

| Mode | Field of View [pixels] (arcmin) | Timing Resolution [ms] |
|---|---|---|
| Full Frame | 398 × 384 (27.2 × 26.2) | 73.3 |
| Extended Full Frame | 398 × 384 (27.2 × 26.2) | 199.2 |
| Large Window | 198 × 384 (13.5 × 26.2) | 47.7 |
| Small Window | 63 × 64 (4.3 × 4.4) | 5.7 |
| Timing | 199 × 64 (13.6 × 4.4) | 0.03 |
| Burst | 20 × 64 (1.4 × 1.4) | 0.007 |

The pn camera has six standard readout modes: full frame (FF), extended full frame, large window (LW), small window (SW), timing, and burst mode (Strüder et al., 2001). These modes utilise different numbers of CCDs and so have varying fields of view and timing resolution, as shown in Table 2.1. Full frame and extended full frame both utilise all 12 CCDs of the pn, while extended full frame mode has a longer integration time, making it ideal for observing extended objects such as

clusters of galaxies (Strüder et al., 2001). Large and small window modes employ reduced fields of view to improve the timing resolution limit and pile-up (see Section 2.2) for bright sources (Strüder et al., 2001). Large window mode operates all four quadrants of the CCDs while reducing the area of each chip. Small window mode utilises the reduced area of only a single detector. Timing and burst modes both operate a single CCD chip and are useful for observing sources with extremely high count rates (Strüder et al., 2001). Timing mode operates in only one dimension, collapsing the data and reading out a single row of the CCD, while burst mode yields an even faster timing resolution at the expense of collecting light for only 3% of the operating time.
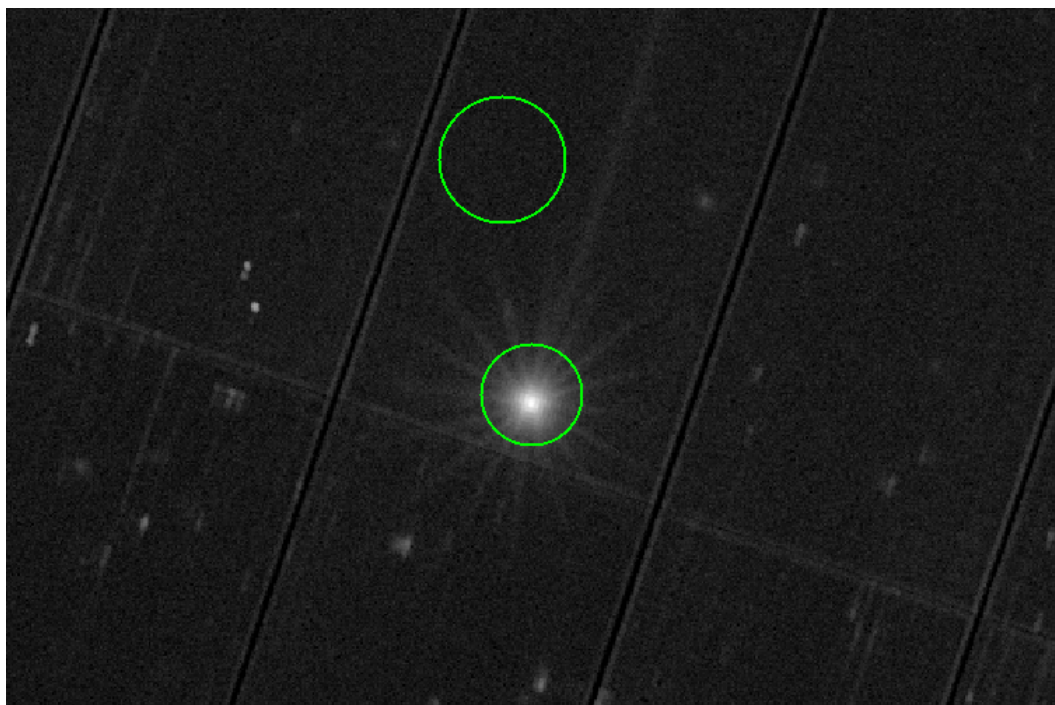


Figure 2.1: Raw image of Markarian 335 with pn camera in full frame mode showing the source and background extraction region used in this work.

A raw image of Markarian 335 taken by the pn camera in full frame mode is shown

in Figure 2.1. The division of individual CCD chips on the detector are visible, as are some bad pixels and columns. The source is centred.

All data utilised in this analysis were taken by the EPIC-pn detector to take advantage of the large effective area of the telescope, which yields a high enough count rate for a thorough analysis (Wilkins and Gallo, 2015a). Additionally, the use of a single detector removes the necessity to cross-calibrate multiple detectors.

## 2.2 OBSERVATIONS AND DATA PROCESSING

For this work, five sets of archival data of Markarian 335 from the *XMM-Newton* pn detector were analysed. An observation of Mrk 335 taken in 2000 in a high state was not used in this analysis, as pileup was examined and found to be significant in that observation. Information on the five observations analysed is listed in Table 2.2. Good Time Interval (GTI) indicates the length of the observation for which there is good data (i.e. no background flaring).

Table 2.2: *XMM-Newton* observations of Mrk 335 analysed in this paper, indicating the name each observation will be referred to as henceforth.

| Obs ID | Reference Name | Start Date | Rev | Exposure | Mode | Filter | GTI (ks) |
|--------|----------------|------------|-----|----------|------|--------|----------|
| 0306870101 | XMM-High | 2006-01-03 | 1112 | 133 ks | SW | THIN1 | 133 |
| 0510010701 | XMM-Low1 | 2007-07-10 | 1389 | 22.6 ks | LW | THIN1 | 17 |
| 0600540601 | XMM-Int1 | 2009-06-11 | 1741 | 132 ks | FF | THIN1 | 115 |
| 0600540501 | XMM-Int2 | 2009-06-13 | 1742 | 82.6 ks | FF | THIN1 | 80 |
| 0741280201 | XMM-Low2 | 2015-12-30 | 2941 | 140 ks | FF | THIN1 | 118 |

The data were downloaded from the *XMM-Newton* Science Archive[1] as Observational Data Files (ODFs) and processed using the Science Analysis System (SAS) software version 15.0.0 developed by the European Space Agency. The command `epchain` was employed to process the ODFs and create an event list from the raw data and spacecraft information. An event list contains information for every photon collected during the observation, from which images, light curves, and spectra can be created. It lists the time of arrival as well as the position and energy of each photon detected.

The data were then checked for background flaring and pileup. High background

---

[1]`http://nxsa.esac.esa.int/`

radiation, solar radiation, and the Earth's radiation belts can all contribute to flaring

in the background that can diminish data quality (Figure 2.2). Pile-up occurs when

more than one photon strikes a pixel before a read-out cycle of the CCD can be

completed. If this occurs, two photons of a lesser energy can be mistaken for a single,

higher-energy photon. The spectrum will appear harder than it is and the count rate

will be underestimated if this occurs frequently throughout an observation [2].
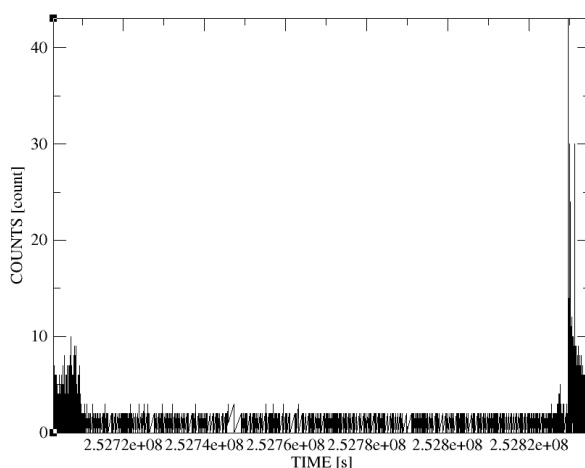


Figure 2.2: Histogram of the background light curve for XMM-High, showing periods of flaring at the start and end of observation. These segments are omitted in analysis.

To check for these effects, first the source and background regions had to be

extracted. This was done visually using the program *SAOImage DS9*[3]. For each

observation, source spectra were extracted from a circular region 35 arcsec in diameter

and centred on the source. Background spectra were extracted from a circular region

50 arcsec in diameter in order to achieve a high signal-to-noise ratio (Kammoun

et al., 2015). The background annuli were taken from the same chip as the source,

as close to the source as possible while avoiding contamination from the source and

---

[2]SAS Cookbook: `http://heasarc.gsfc.nasa.gov/docs/xmm/abc/node9.html`
[3]`ds9.si.edu/`

the readout streak. Figure 2.1 displays the background and source extraction regions. The background light curves were examined for flaring and such periods were omitted in the analysis (see Figure 2.2).

Pileup in the five analysed observations was also found to be negligible (see Figure 2.3). Background-corrected light curves were created using the command `epiclccorr`, subtracting the background from the source, ignoring any periods of background flaring as well as bad pixels, and considering only single and double events.
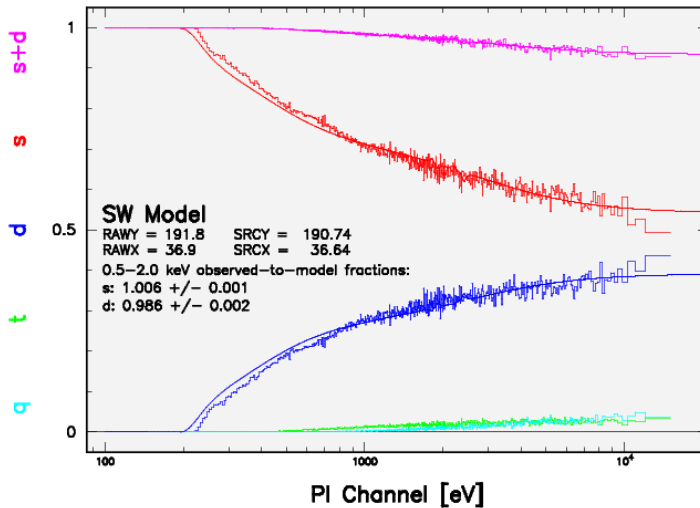


Figure 2.3: Data compared to pileup models, indicating a good fit.

Source and background spectra were created from the event list using the same extraction regions, again considering only single and double events and omitting bad pixels. EPIC response matrices were generated using the SAS tasks ARFGEN and RM-FGEN to construct the ancillary response matrices (ARF) and photon redistribution matrices (RMF), respectively. The energy channels were binned using GRPPHA such that each bin contained a minimum of 20 counts in order to apply Poisson statistics.

# Chapter 3

# ANALYSIS & RESULTS

## 3.1   SELECTING APPROPRIATE ENERGY BANDS

To construct a Flux-Flux Plot one must first choose the energy bands to compare. These bands can be chosen such that they represent different components contributing to the AGN spectrum. The Flux-Flux Plots constructed by Kammoun et al. (2015) compared an energy band representative of the continuum emission to non-continuum emission at higher and lower energies. This method was adopted for this work, and so the first step was to identify the energy band that best represented the continuum emission. To do this, the spectra of the first four observations (XMM-High, XMM-Low1, XMM-Int1, XMM-Int2) were loaded into the X-ray spectral modelling software XSPEC [1]. Because the continuum emission arises from Comptonisation and takes the form of a power-law, the spectra were each fit with an absorbed power-law using the model `tbabs*powerlaw`. Galactic absorption was considered, with a hydrogen column density to Markarian 335 of $N_H = 3.56 \times 10^{20}$ cm$^{-2}$ (Kalberla et al., 2005).

Figure 3.1 shows the absorbed power-law model fit to 1 - 2 keV and extrapolated between 0.3 - 10 keV for each of the first four observations. The bottom panel shows the residuals of the fits. From the residuals, it is clear that the energy band from 1 -

---

[1]`https://heasarc.gsfc.nasa.gov/xanadu/xspec/`

2 keV is well-fit with an absorbed power-law, while the model deviates at higher and lower energies. As such, 1 - 2 keV was chosen to be representative of the continuum emission for Markarian 335. Additionally, other energy ranges (e.g. 1.1 - 3 keV) were fit with the absorbed power-law model, and all ranges tested indicated that 1 - 2 keV was the band that best represented the continuum emission. The continuum emission is indicated in Figure 3.1 by the yellow band.
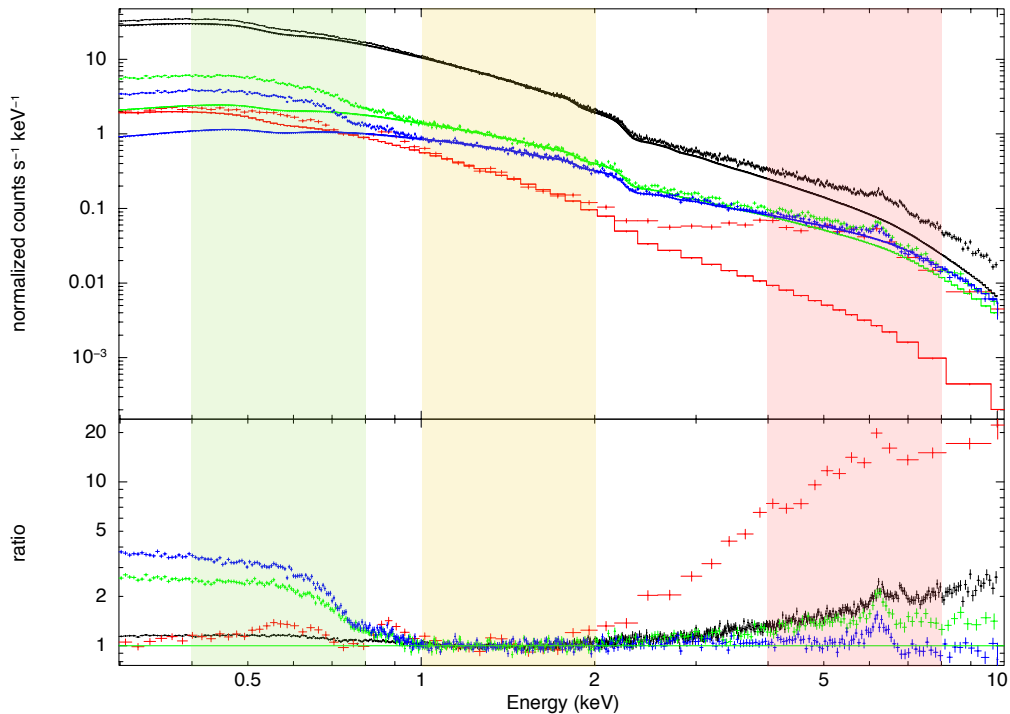


Figure 3.1: First four XMM spectra (black, red, blue, green, respectively) fit with an absorbed power-law from 1 - 2 keV and extrapolated from 0.3 - 10 keV. Energy bands indicating the soft excess, continuum, and hard excess are shown in green, yellow, and red respectively.

The soft band to use in the Flux-Flux Plots was chosen such that it represented the soft excess of Markarian 335. The soft excess is the low-energy regime which

exhibits higher flux than can be obtained from merely a power-law. This component can be attributed to relativistically blurred reflection from the disc (Ross and Fabian, 2005), a second Comptonisation layer (Done et al., 2012), or modified spectral shape from an ionised absorber (Gierliński and Done, 2006).

Uttley et al. (2004) and Ponti et al. (2006) note that having well-separated bands when constructing a Flux-Flux Plot reveals the most spectral variability. As such, when identifying the soft and hard bands to be used in this analysis, they were chosen such that there was a gap between these bands and the continuum band. From the spectral fits shown in Figure 3.1, 0.4 - 0.8 keV was chosen as the soft band (green strip Figure 3.1). The hard band was chosen to be 4 - 8 keV (red strip Figure 3.1).

## 3.2    BINNING IN FLUX AND TIME

### 3.2.1    FLUX-FLUX PLOT BINNING

When constructing a Flux-Flux Plot from two light curves, there can be a lot of scatter present in the data. Figure 3.2 shows a Flux-Flux Plot for XMM-High constructed from light curves binned at 500s (grey data points), and the scatter is apparent. Flux-Flux Plots are typically binned-up after being constructed in order to reduce scatter, improve the signal to noise ratio, and better examine fit statistics (Taylor et al., 2003). The binned-up data are denoted by the black markers in Figure 3.2.
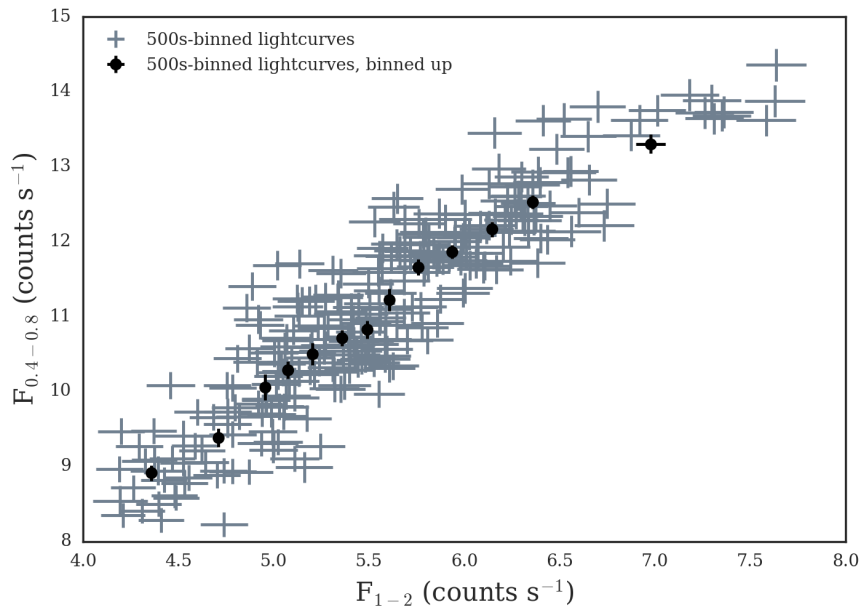


Figure 3.2: Soft vs Continuum FFP for XMM-High constructed from light curves binned at 500s (grey). The black circles denote the binned-up data with at least 20 points per bin.

While binning-up the data for Markarian 335 it was noted that the shape of the data differed depending on if it was sorted by the x-dimension or the y-dimension.

Sorting by different dimensions when binning the data produced different shapes of the data and so conflicting fit parameters. Figure 3.3 compares the 500s-binned light curve data for XMM-High binned-up by sorting the x-dimension first (blue circles) and sorting the y-dimension first (red squares). Linear fits to the data binned in each dimension yield parameters that do not agree with one another within uncertainty (fit parameters shown in Figure 3.3).
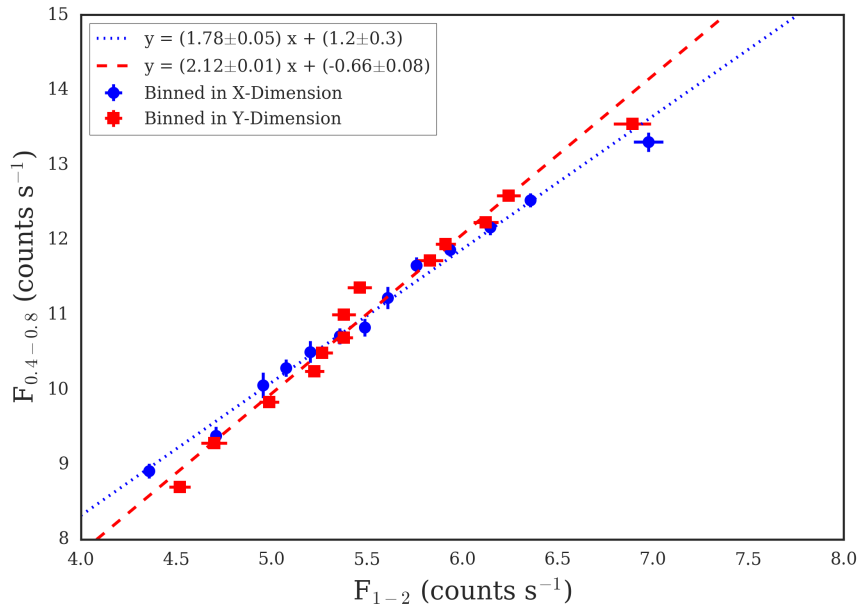


Figure 3.3: XMM-High FFP showing data binned-up by different axes and the fits obtained for each binning approach.

To further examine the implications of binning-up the FFPs, simulations were run using XSPEC. A simple power-law model was created using `cpflux*po`. `cpflux` was employed in order to keep the integrated flux constant. Since the photon index and normalisation are intrinsically linked, the variation of one of these parameters affects the other and so must be taken into account when varying parameters. A script was written to vary a single parameter of the power-law, either photon flux (in lieu of

normalisation) or photon index. A Gaussian random number generator was used to

vary between physical values of these parameters, and the flux in the three chosen

bands was output. From this, FFPs were created that result from the variation of a

single parameter in a power-law model.

Figure 3.4a displays the FFP resulting from varying only the normalisation (or

photon flux, when using `cpflux`) of a simple power-law model. The resulting FFP,

shown in grey is linear, as is expected. The data were then binned-up by sorting the x-

dimension first. They were also binned up by sorting in the y-dimension. Comparison

of the two sets of binned-up data reveals that they are identical.

The same was found when only the photon index was varied in the power-law

model, as shown in Figure 3.4b. Varying only the photon index produces a power-

law shaped FFP, as expected, which is identical whether binned-up by the x- or

y-dimension.



(a) Varied Normalisation                (b) Varied Photon Index
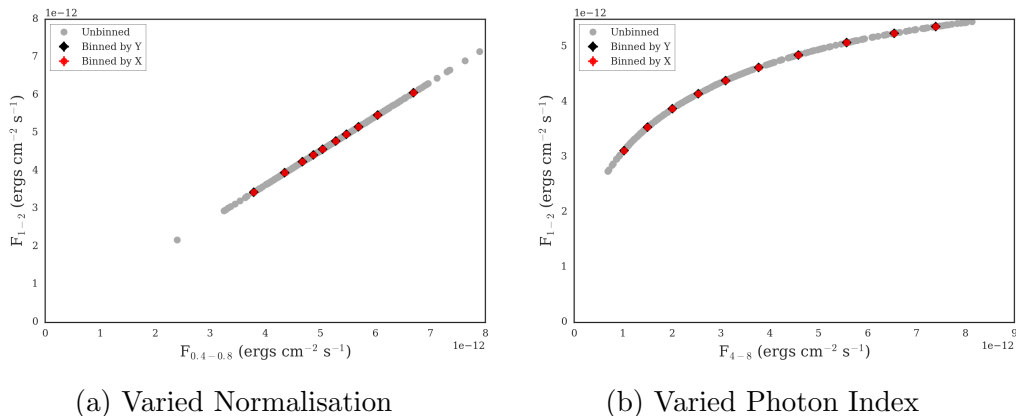
Figure 3.4: FFPs resulting from varying a single parameter of a power-law model, binned up by both x- and y-dimensions. Varied normalisation is shown in panel A while panel B depicts varied photon index.

Next, both the normalisation and photon index parameters of the power-law model

were varied independently. The resulting FFP, shown in Figure 3.5 exhibits clear scatter. When the data were binned-up by sorting the x-dimension, the result was clearly different than that obtained by sorting the y-dimension.
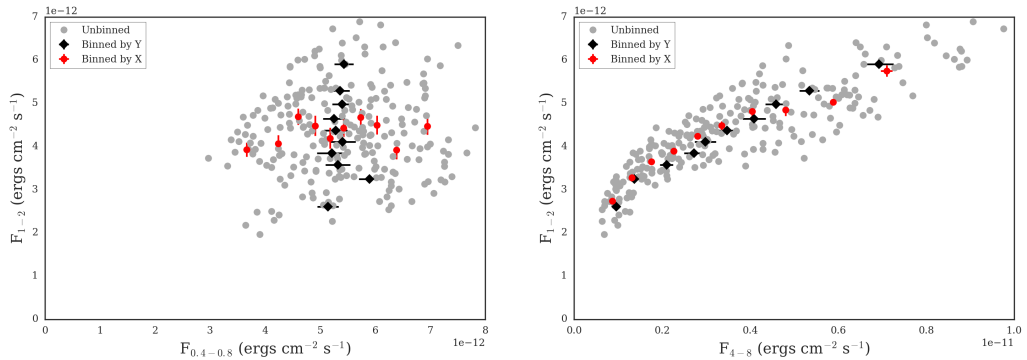


Figure 3.5: FFPs resulting from varying both photon index and normalisation of a simple power-law model, binned-up by both x- and y-dimensions.

If the FFP is well-represented by a linear or power-law distribution (i.e. only one model component is varying), then binning the data up in the FFP is not affected by the dimension it is binned by. However, if there is more than one model component varying independently, the resulting FFP exhibits scatter and so yields different results when binned by different dimensions.

Since the FFP made for Mrk 335 clearly showed different results when binning-up by different dimensions, it can be concluded that there is more than one parameter independently varying over the course of the observations.

As such the FFPs were not binned-up in the flux domain, and the data were binned *only* in time by binning-up the light curves prior to constructing the FFPs.

### 3.2.2   LIGHT CURVE BINNING

Since the data were only to be binned in time by binning-up the light curves, finding the optimal time-binning of the light curves was an important consideration. To determine what time-binning to use, many FFPs were constructed using light curves of different time-binning. Light curves of 100s, 500s, 1ks, and 2ks were investigated.

Figure 3.6 shows the FFP of the continuum band vs. soft band for XMM-High constructed using light curves of different time-binning. Linear fits were made to the plots in order to compare the light curves of different time binning. As the fit parameters in Figure 3.6 show, the different binned light curves agree within uncertainty with the exception of the 100s binned data. The same trend was seen in all observations for both hard and soft bands.
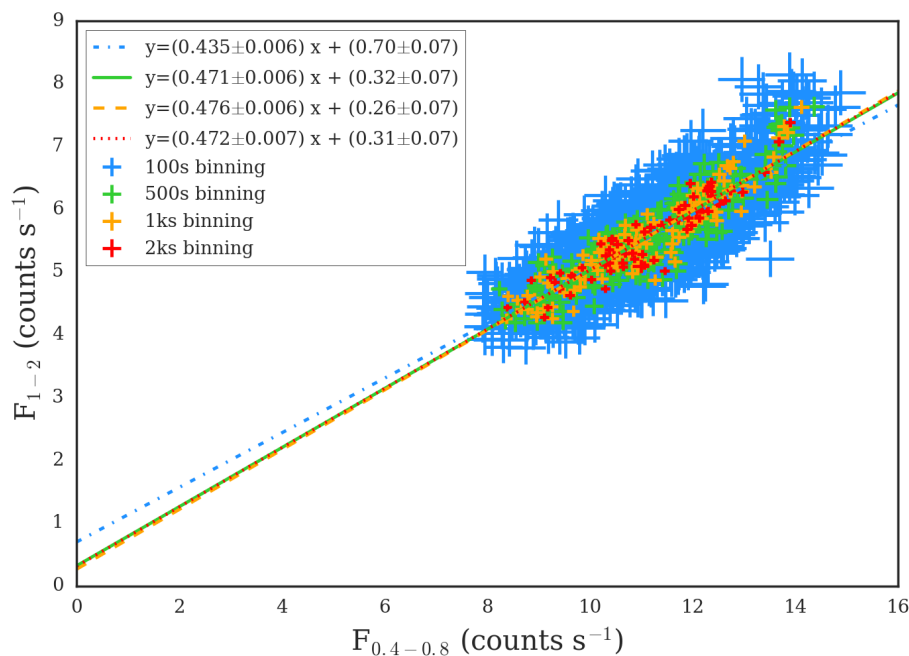


Figure 3.6: FFP of XMM-High comparing the effects of light curve binning.

From these comparisons, it was determined that 1ks time-binned light curves would be utilised for the investigation. This was optimised to achieve a good signal-to-noise ratio while retaining resolution of short-term variability in the light curve.

The 1ks-binned light curves used to construct the FFPs are shown for each observation in Figures 3.7-3.11.
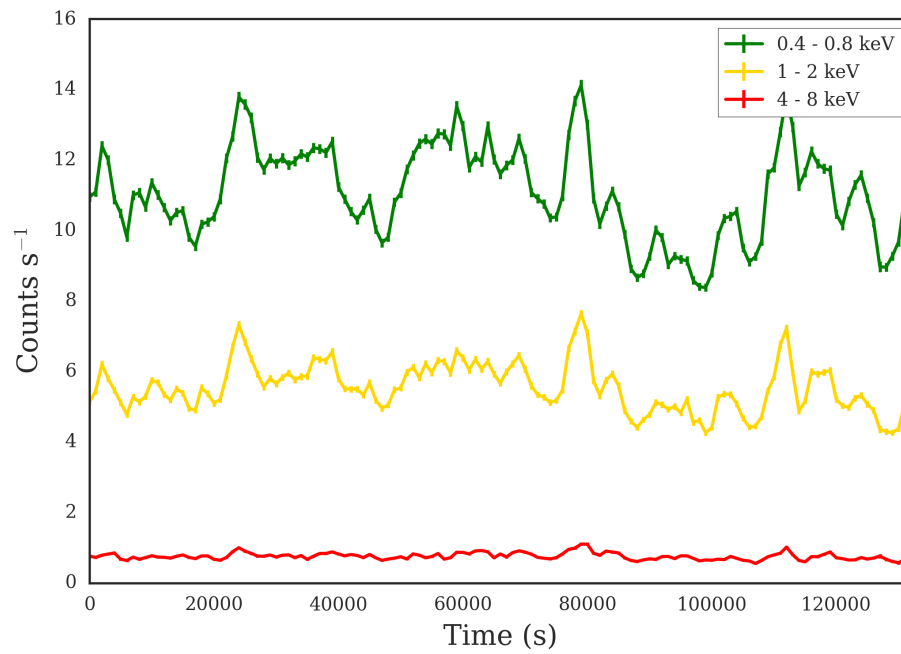


Figure 3.7: Light curves of the hard, continuum, and soft bands for XMM-High.
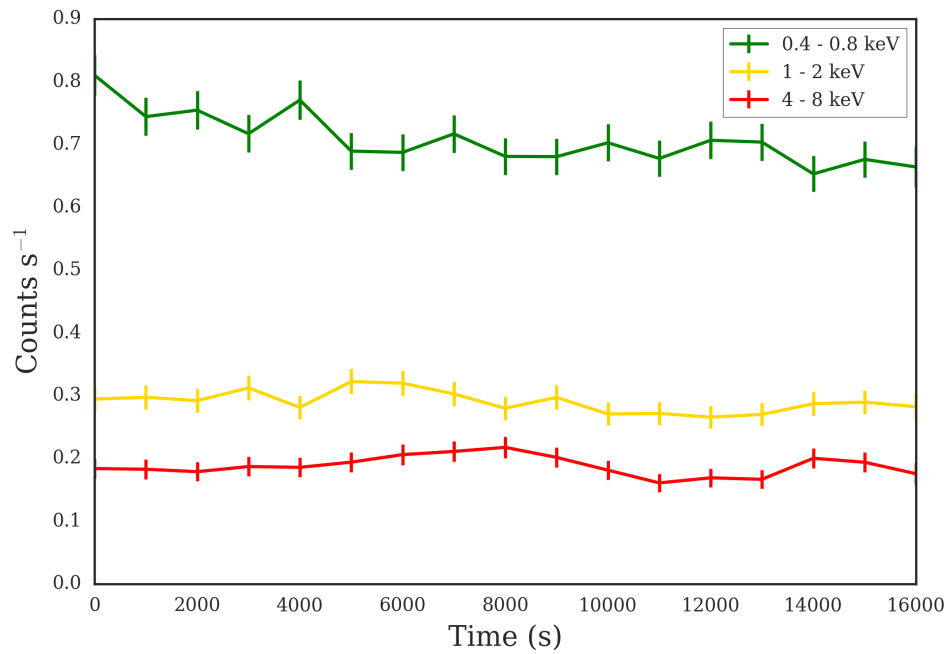
Figure 3.8: Light curves of the hard, continuum, and soft bands for XMM-Low1.
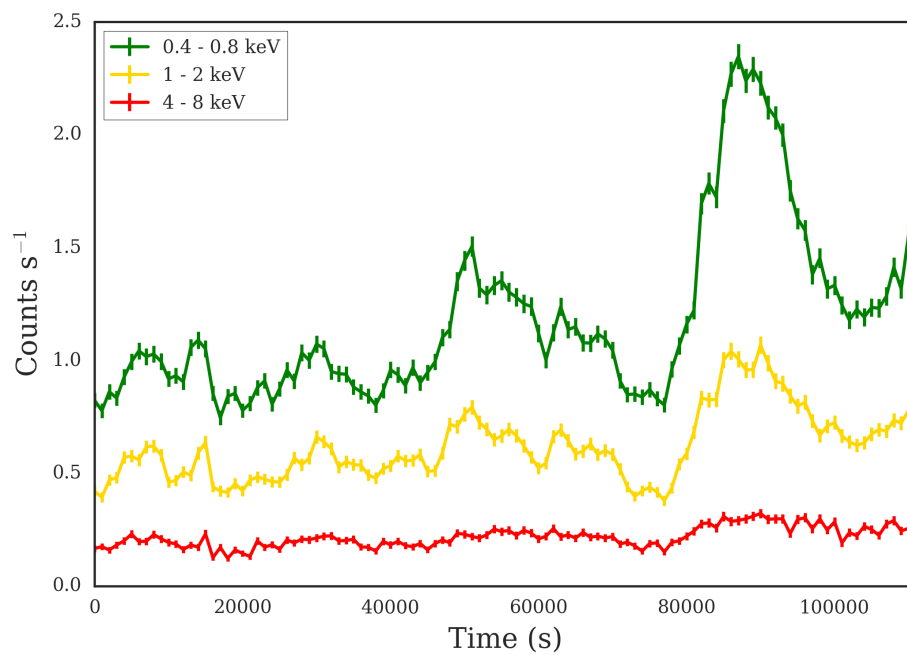


Figure 3.9: Light curves of the hard, continuum, and soft bands for XMM-Int1.
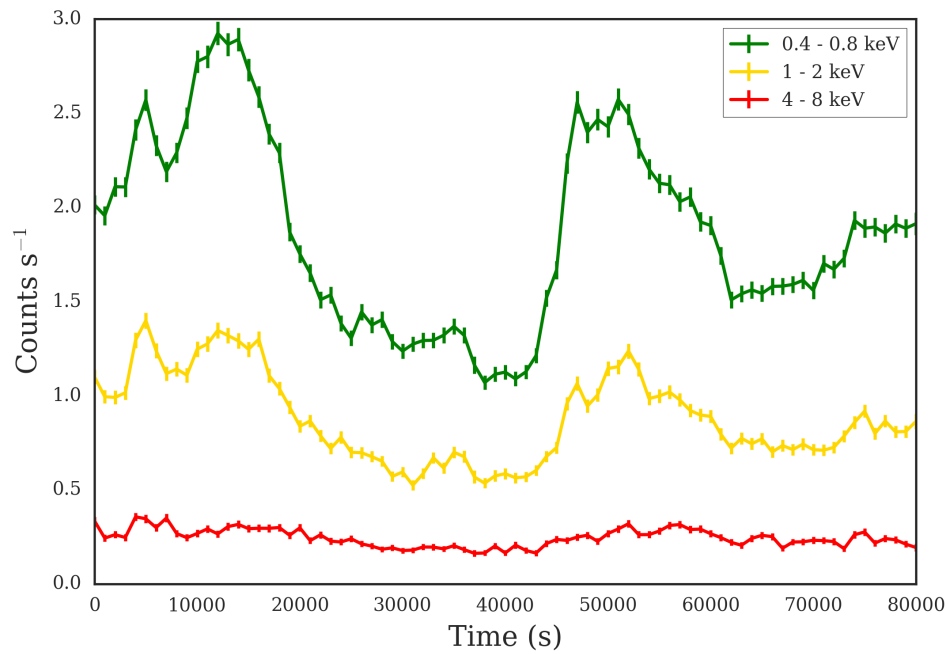
Figure 3.10: Light curves of the hard, continuum, and soft bands for XMM-Int2.
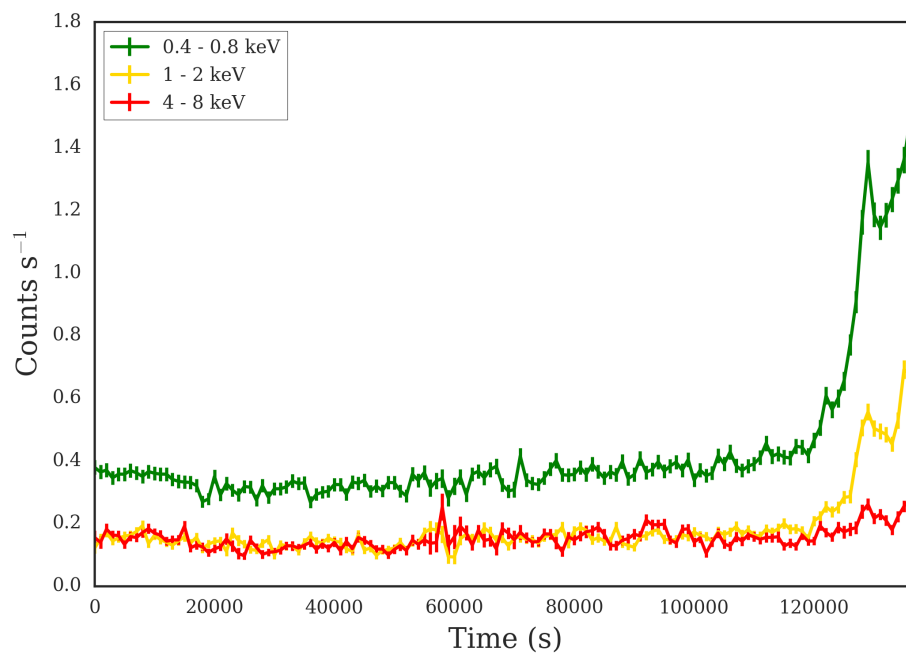


Figure 3.11: Light curves of the hard, continuum, and soft bands for XMM-Low2.

## 3.3 FLUX-FLUX PLOTS

Flux-Flux Plots were constructed of the soft band against continuum and the hard band against continuum for each observation of Mrk 335. The continuum flux was plotted as the independent variable in order to see the changes in both the hard and soft bands relative to the continuum. Linear, power-law and power-law plus constant fits were made to each plot to determine if these simple modes of variability fit the data well. Observations were fit independently to investigate whether the mode of variability is correlated to the overall flux state of the source. FFPs with fits and residuals for hard and soft bands of each epoch are shown in Figures 3.12-3.21.

The parameters of the fits to each Flux-Flux Plot, as well as the goodness-of-fit statistics, are displayed in Tables 3.1-3.5. Parameters correspond to the constants described in Equations 1.1, 1.2, and 1.3.

Figure 3.12: FFP with fits to soft band against continuum for XMM-High, as well as residuals for linear (top), power-law (middle), and power-law plus constant (bottom) fits.

Figure 3.13: FFP with fits to hard band against continuum for XMM-High, as well as residuals for linear (top), power-law (middle), and power-law plus constant (bottom) fits.
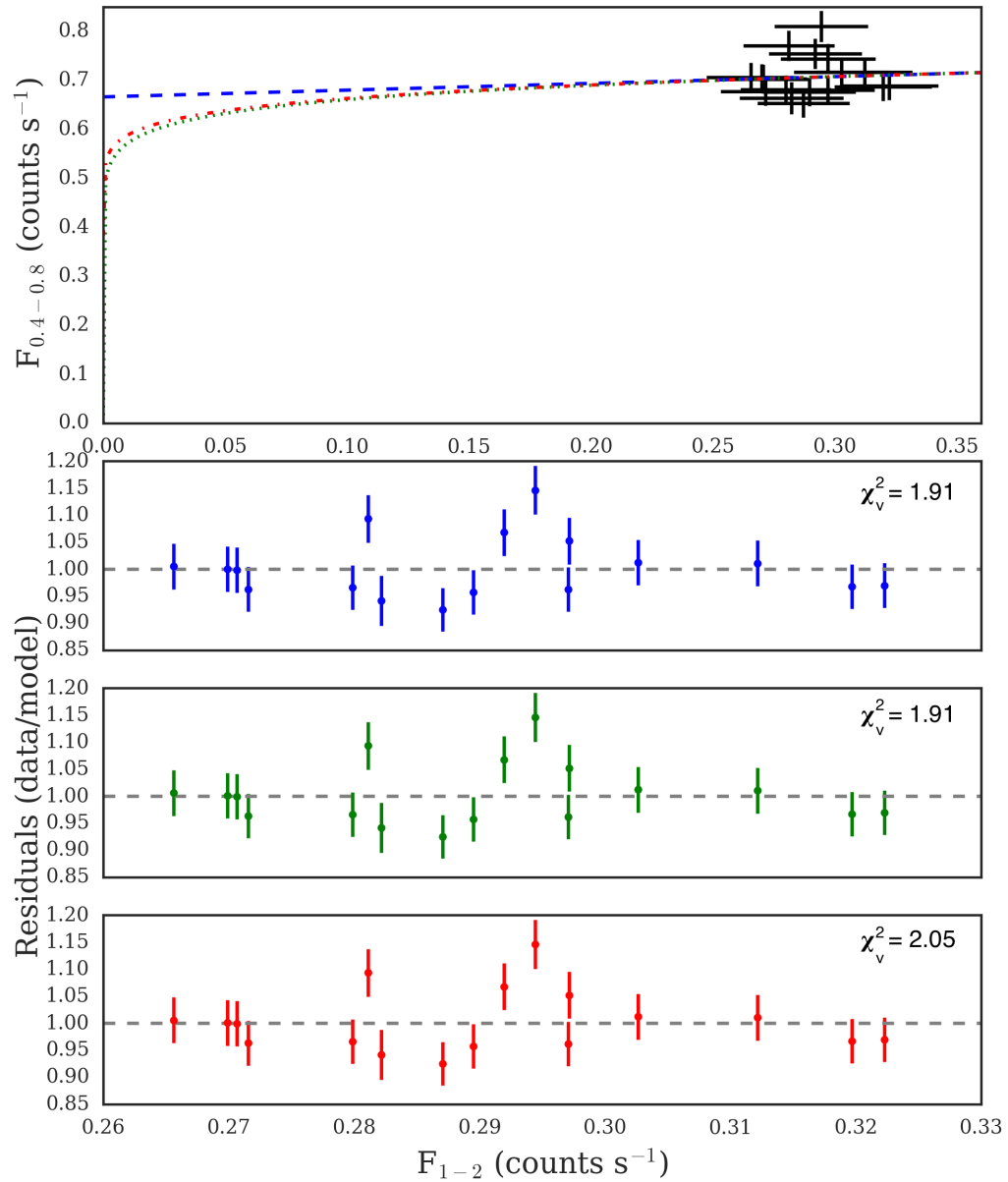
Figure 3.14: FFP with fits to soft band against continuum for XMM-Low1, as well as residuals for linear (top), power-law (middle), and power-law plus constant (bottom) fits.
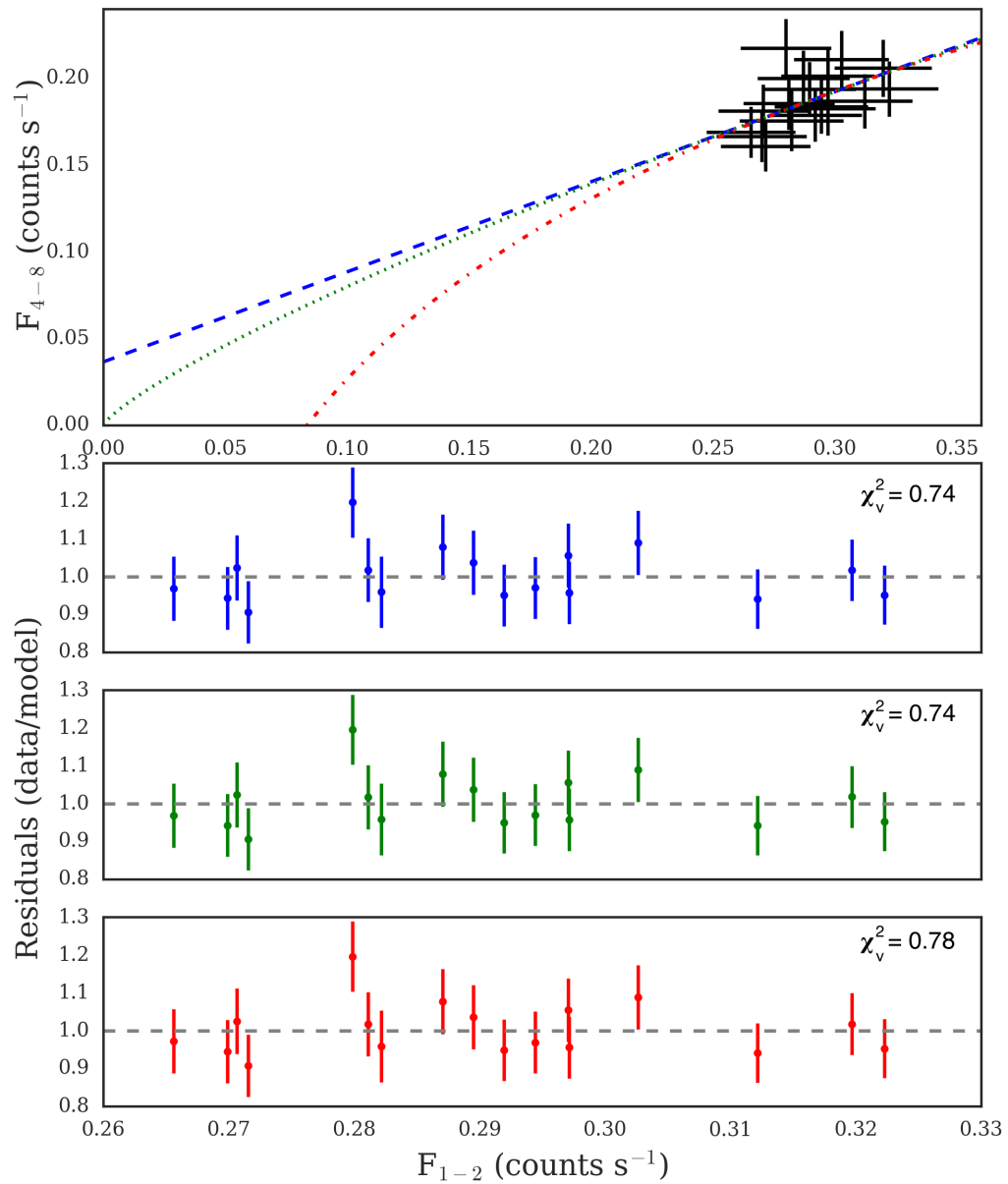
Figure 3.15: FFP with fits to hard band against continuum for XMM-Low1, as well as residuals for linear (top), power-law (middle), and power-law plus constant (bottom) fits.
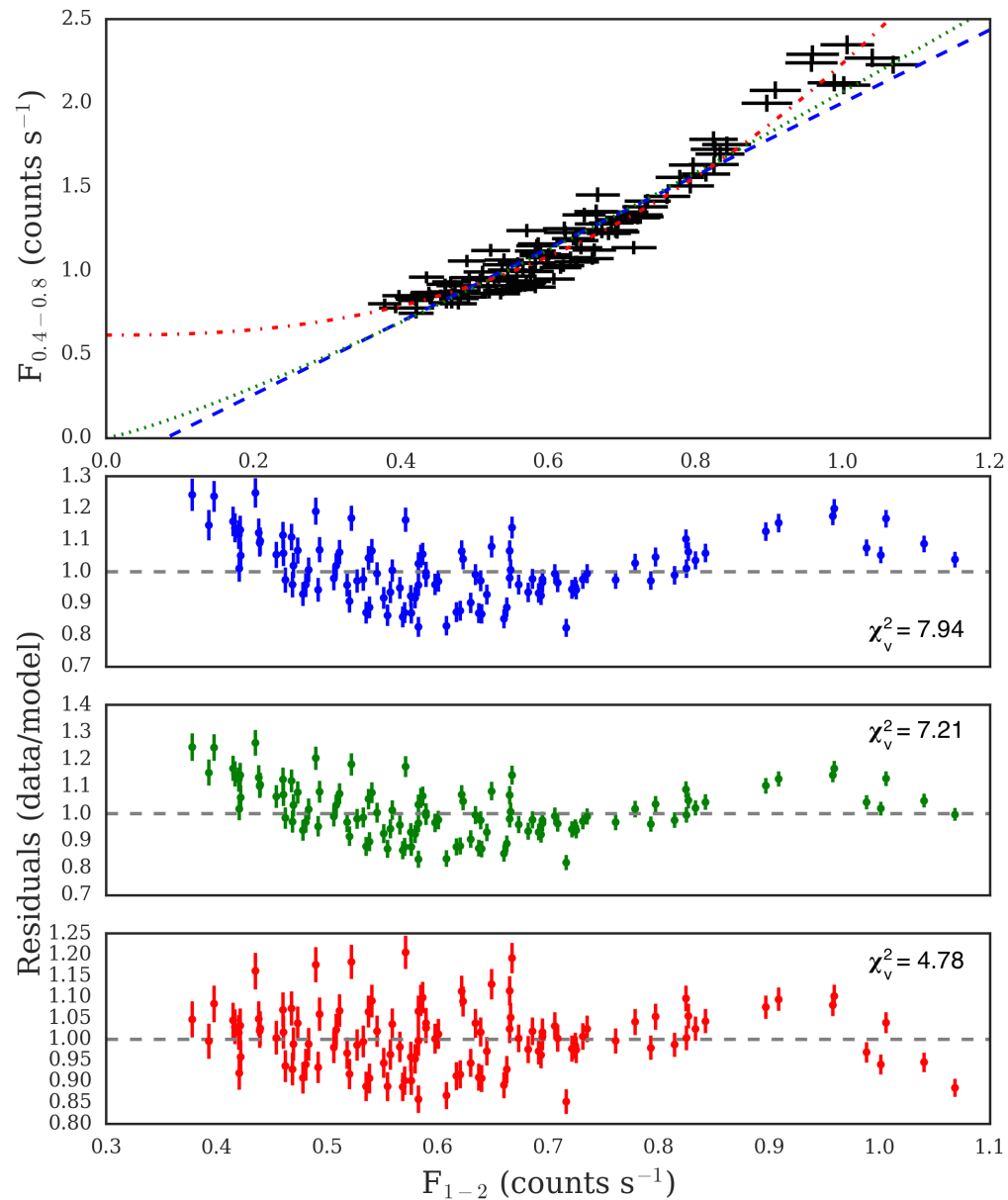
Figure 3.16: FFP with fits to soft band against continuum for XMM-Int1, as well as residuals for linear (top), power-law (middle), and power-law plus constant (bottom) fits.
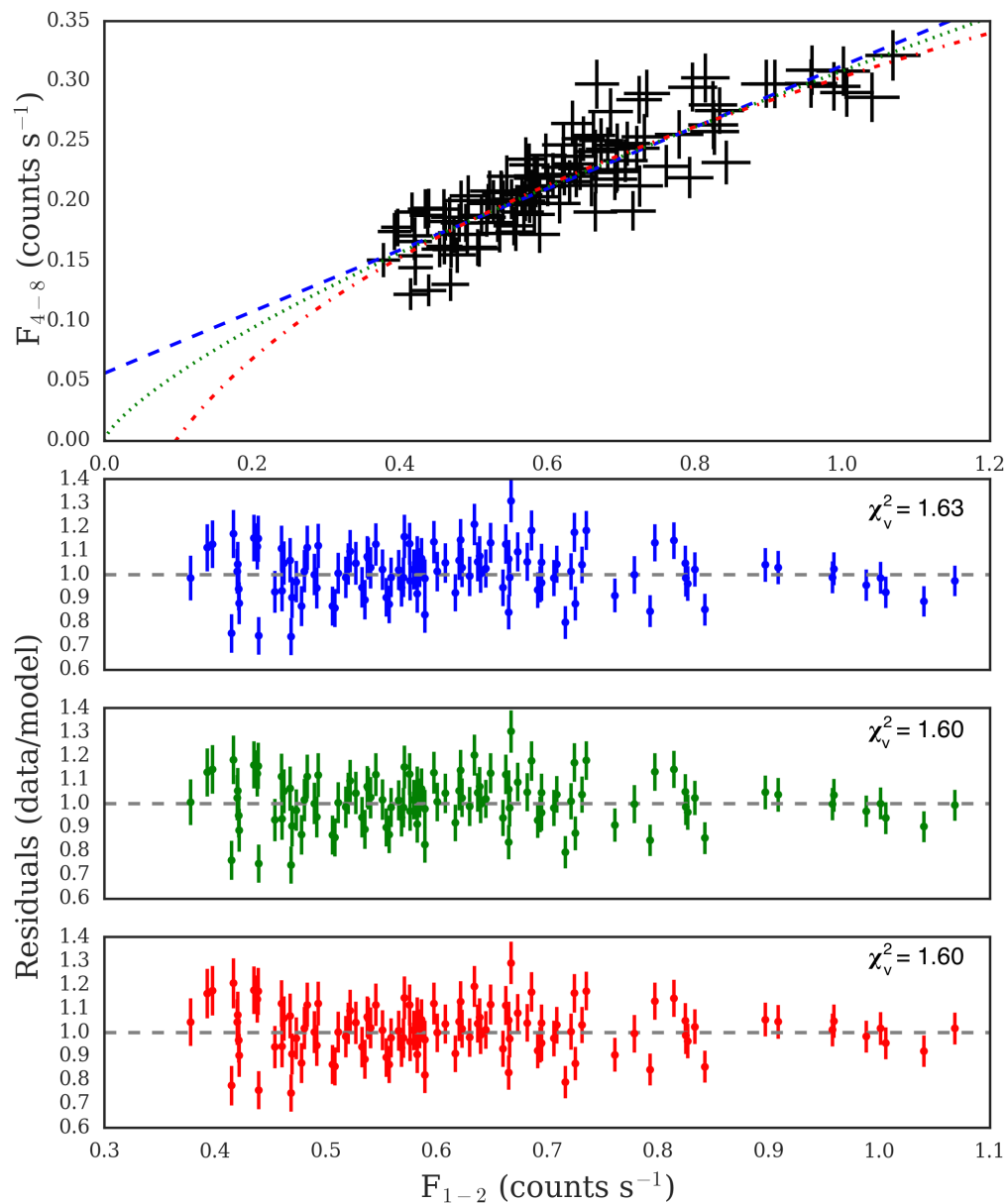
Figure 3.17: FFP with fits to hard band against continuum for XMM-Int1, as well as residuals for linear (top), power-law (middle), and power-law plus constant (bottom) fits.
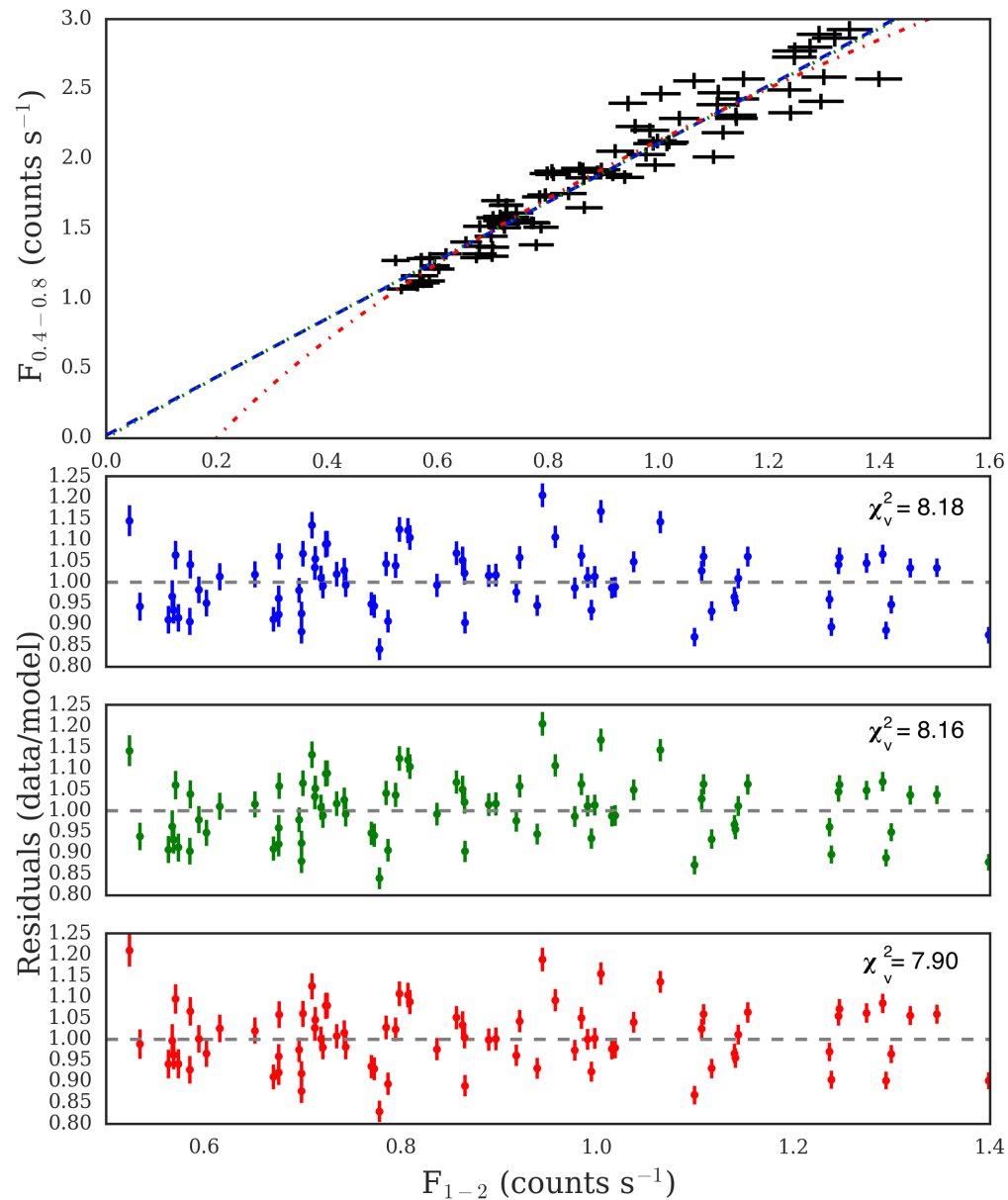
Figure 3.18: FFP with fits to soft band against continuum for XMM-Int2, as well as residuals for linear (top), power-law (middle), and power-law plus constant (bottom) fits.
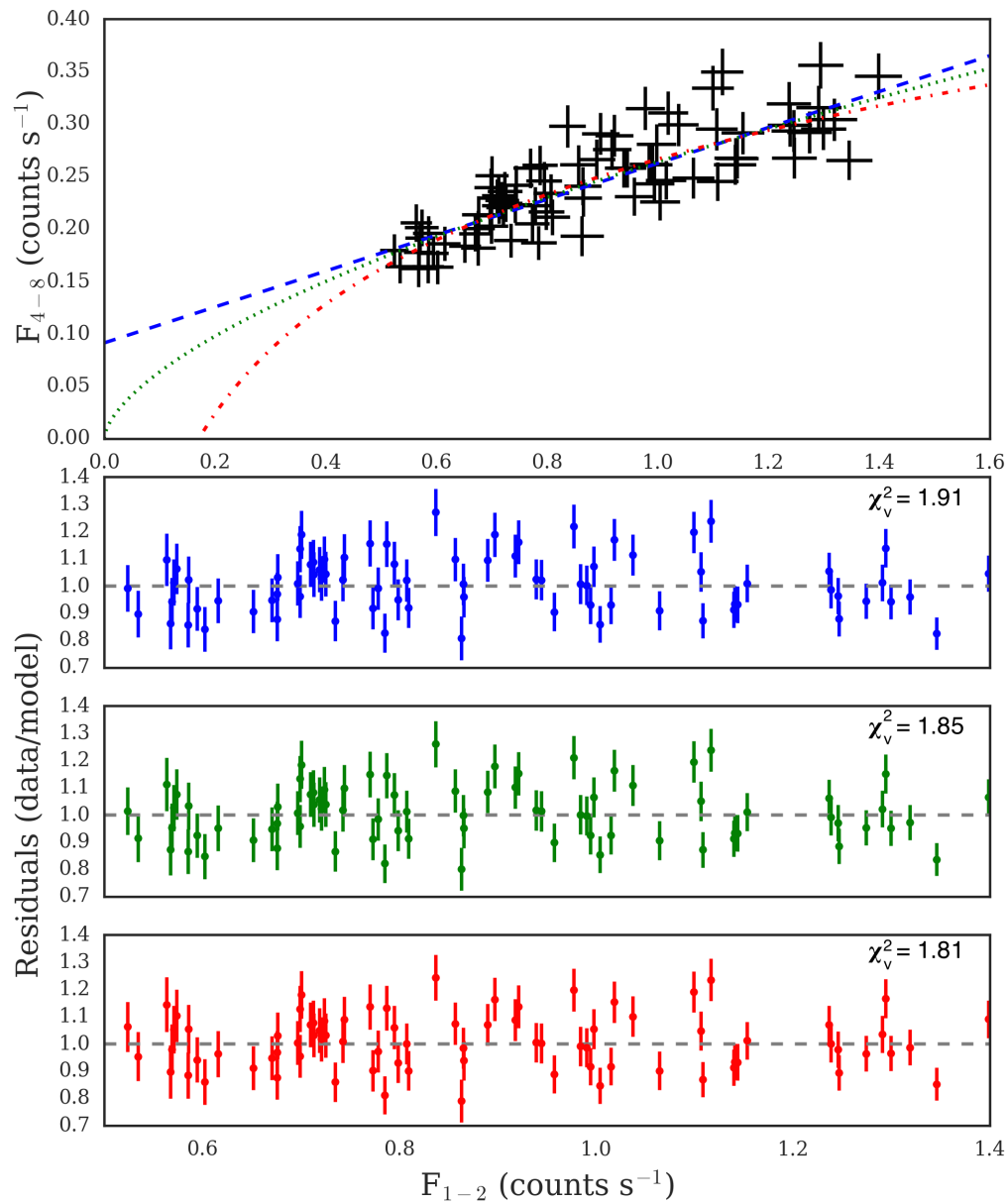
Figure 3.19: FFP with fits to hard band against continuum for XMM-Int2, as well as residuals for linear (top), power-law (middle), and power-law plus constant (bottom) fits.
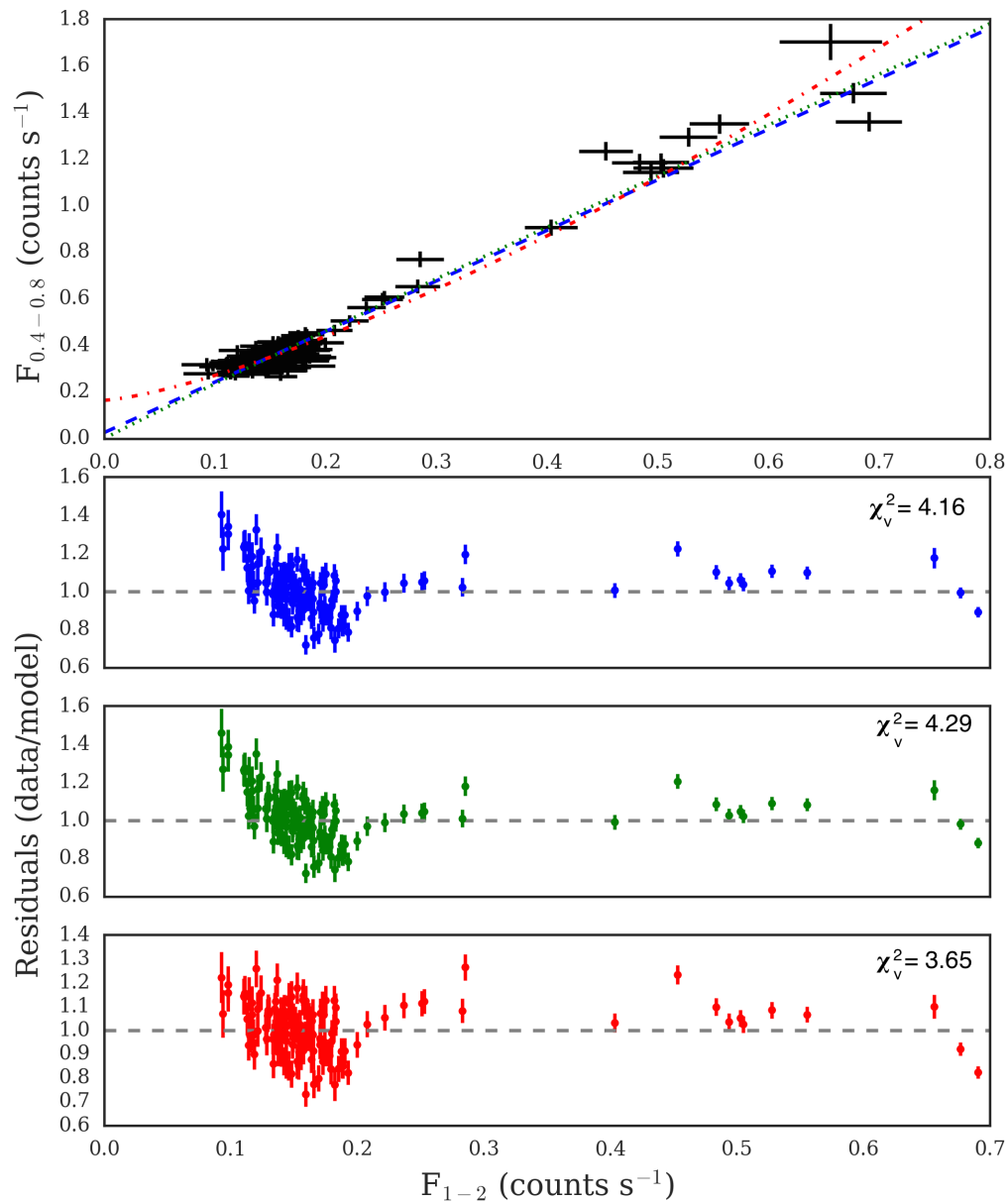
Figure 3.20: FFP with fits to soft band against continuum for XMM-Low2, as well as residuals for linear (top), power-law (middle), and power-law plus constant (bottom) fits.
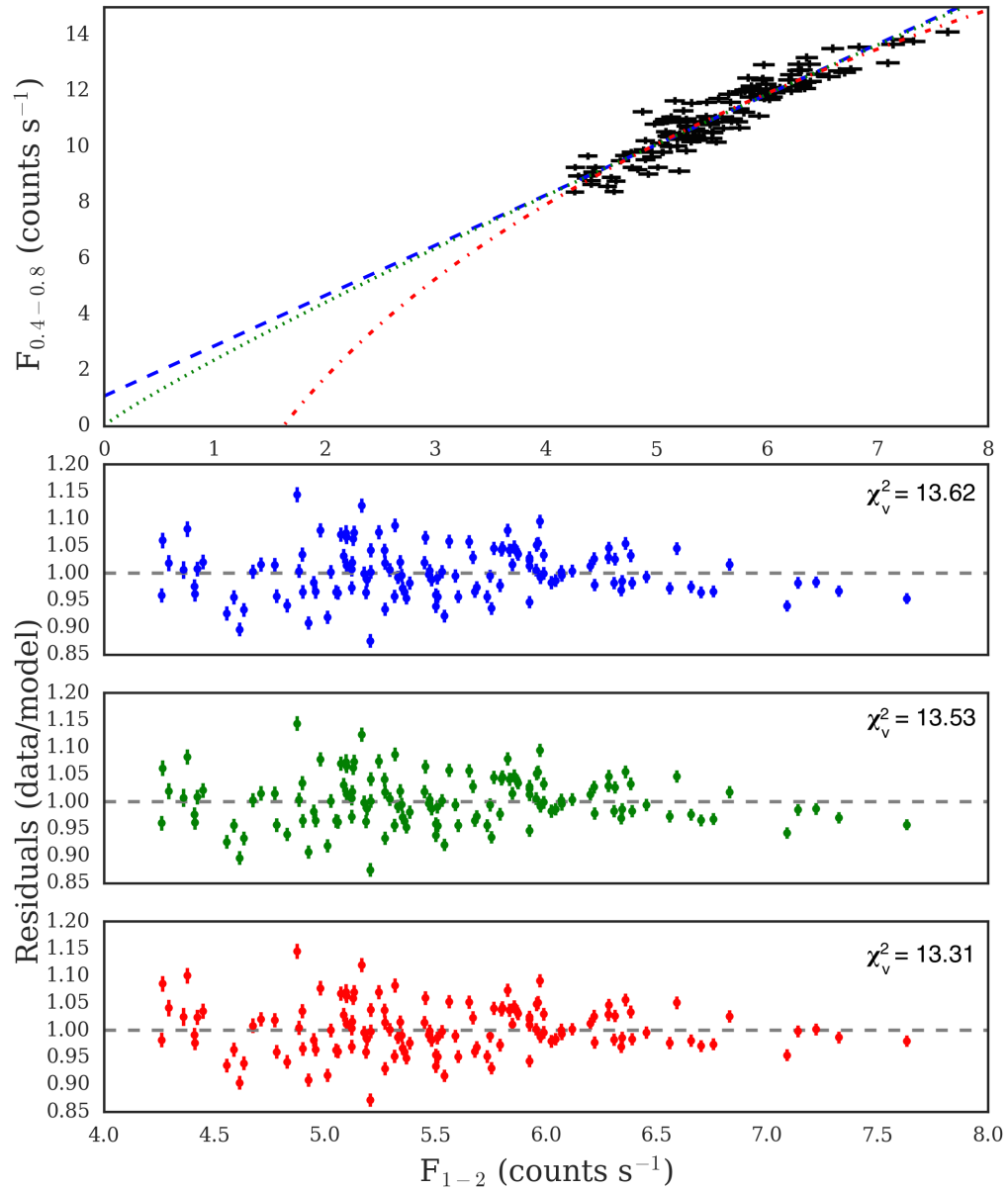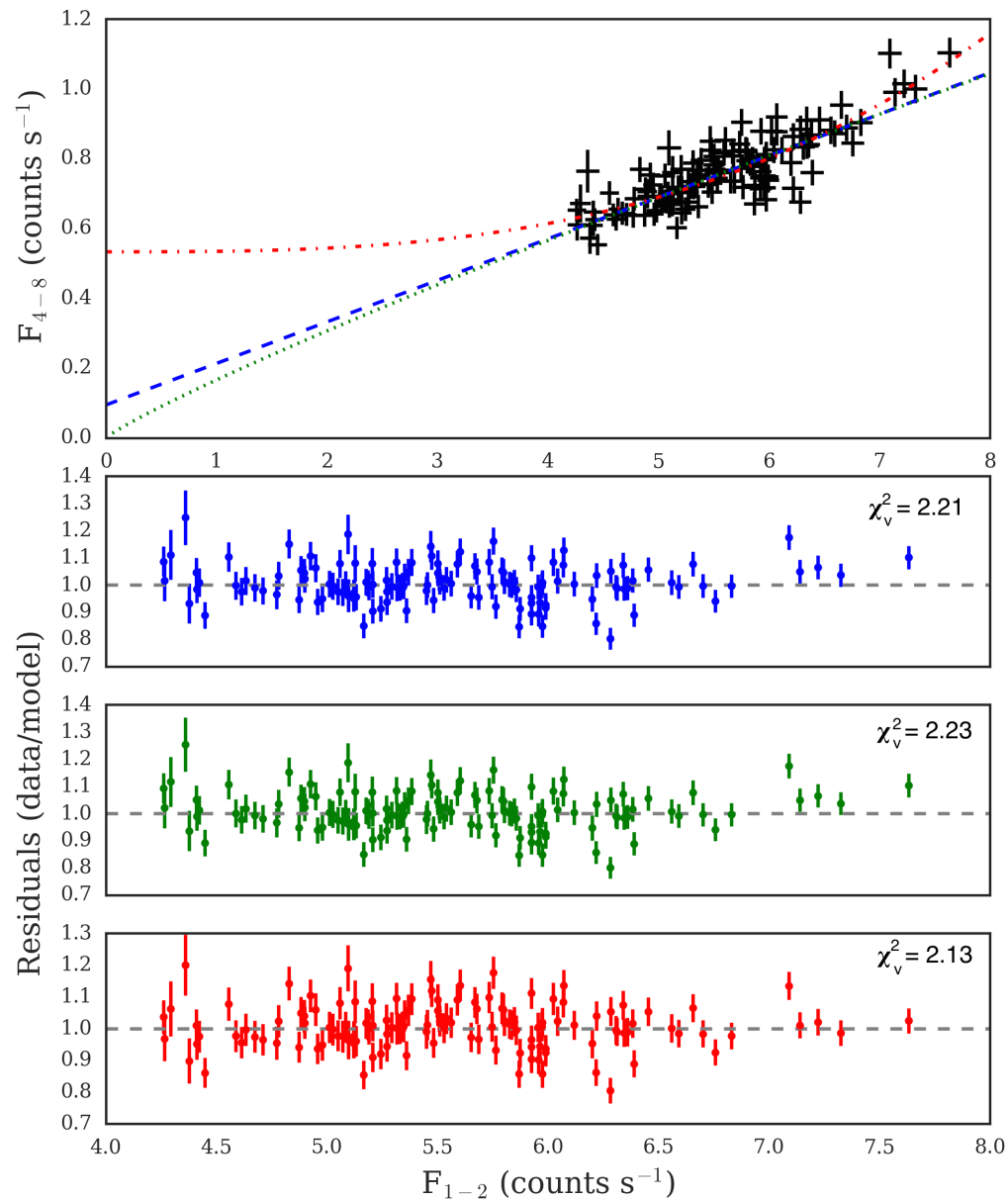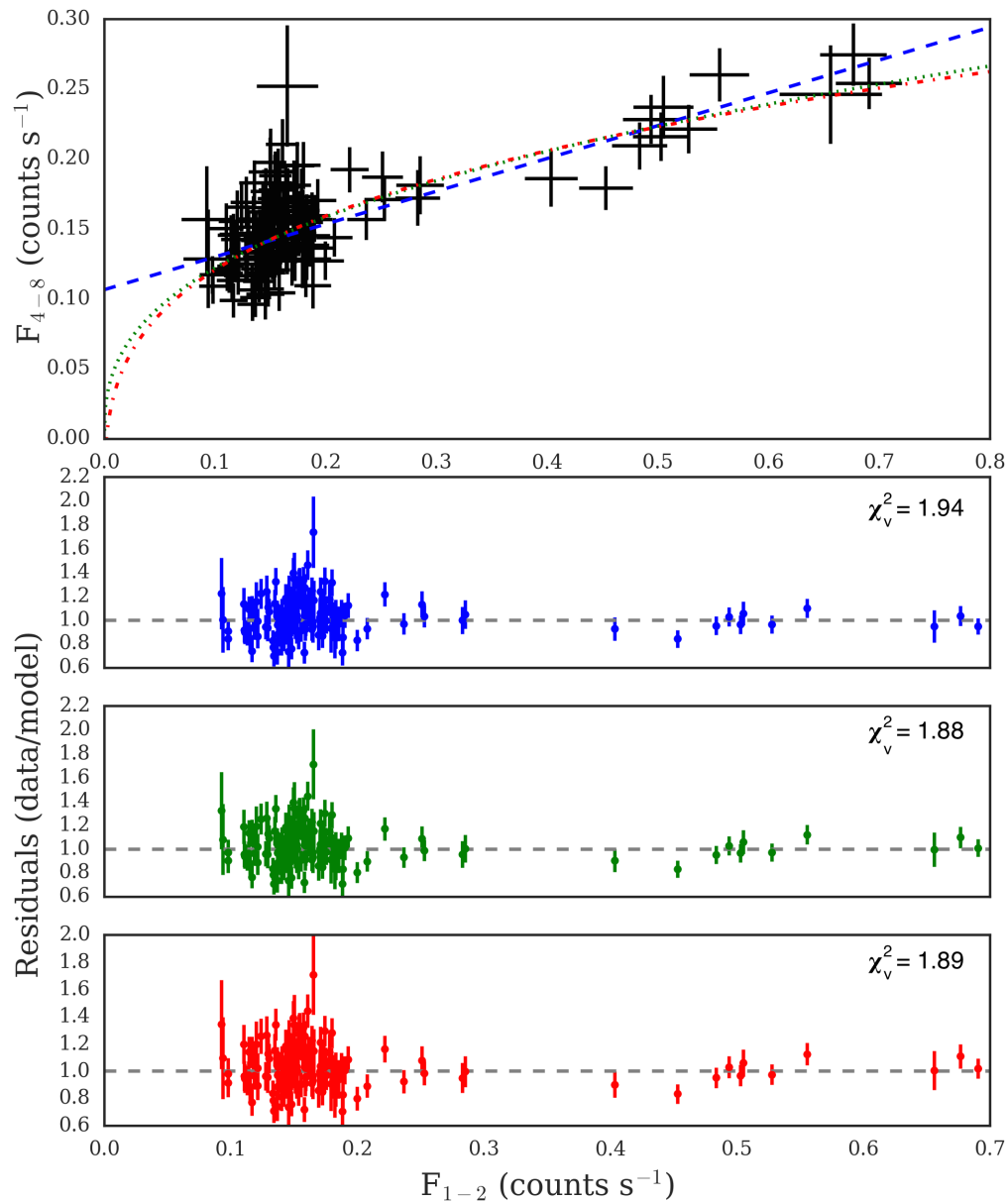
Figure 3.21: FFP with fits to hard band against continuum for XMM-Low2, as well as residuals for linear (top), power-law (middle), and power-law plus constant (bottom) fits.

Table 3.1: Fit parameters for XMM-High FFPs.

| Band vs Continuum | Model | Parameters | $\chi^2$ | DoF | $\chi^2_\nu$ |
|---|---|---|---|---|---|
| soft | linear | m = 1.80 ± 0.01<br>b = 1.1 ± 0.1 | 1784.31 | 131 | 13.62 |
| | power-law | k = 2.37 ± 0.04<br>a = 0.900 ± 0.009 | 1772.15 | 131 | 13.53 |
| | PLc | $\alpha$ = 44.672 ± 0.009<br>$\beta$ = 0.17 ± 15.01<br>c = −48.46 ± 0.01 | 1729.86 | 130 | 13.31 |
| hard | linear | m = 0.119 ± 0.005<br>b = 0.09 ± 0.03 | 289.93 | 131 | 2.21 |
| | power-law | k = 0.17 ± 0.02<br>a = 0.88 ± 0.04 | 291.64 | 131 | 2.23 |
| | PLc | $\alpha$ = 0.001 ± 1.414<br>$\beta$ = 2.951 ± 0.008<br>c = 0.533 ± 0.003 | 276.26 | 130 | 2.13 |

Table 3.2: Fit parameters for XMM-Low1 FFPs.

| Band vs Continuum | Model | Parameters | $\chi^2$ | DoF | $\chi^2_\nu$ |
|---|---|---|---|---|---|
| soft | linear | m = 0.1 ± 0.4<br>b = 0.7 ± 0.1 | 28.66 | 15 | 1.91 |
| | power-law | k = 0.8 ± 0.2<br>a = 0.06 ± 0.18 | 28.64 | 15 | 1.91 |
| | PLc | $\alpha$ = 0.4± 0.1<br>$\beta$ = 0.1 ± 0.2<br>c = 0.4 ± 0.1 | 28.64 | 14 | 2.05 |
| hard | linear | m = 0.5 ± 0.2<br>b = 0.04 ± 0.07 | 11.06 | 15 | 0.74 |
| | power-law | k = 0.5 ± 0.2<br>a = 0.8 ± 0.3 | 11.03 | 15 | 0.74 |
| | PLc | $\alpha$ = 4.713 ± 0.004<br>$\beta$ = 0.03 ± 14.95<br>c = −4.331 ± 0.004 | 10.92 | 14 | 0.78 |

Table 3.3: Fit parameters for XMM-Int1 FFPs.

| Band vs Continuum | Model | Parameters | $\chi^2$ | DoF | $\chi^2_\nu$ |
|---|---|---|---|---|---|
| soft | linear | m = 2.18 ± 0.03<br>b = −0.18 ± 0.02 | 872.98 | 110 | 7.94 |
| | power-law | k = 2.06 ± 0.01<br>a = 1.20 ± 0.01 | 793.11 | 110 | 7.21 |
| | PLc | $\alpha$ = 1.62 ± 0.02<br>$\beta$ = 2.44 ± 0.08<br>c = 0.61 ± 0.02 | 521.34 | 109 | 4.78 |
| hard | linear | m = 0.26 ± 0.01<br>b = 0.056 ± 0.007 | 179.41 | 110 | 1.63 |
| | power-law | k = 0.308 ± 0.005<br>a = 0.74 ± 0.03 | 176.15 | 110 | 1.60 |
| | PLc | $\alpha$ = 0.5 ± 0.03<br>$\beta$ = 20.4 ± 0.3<br>c = −0.2 ± 0.3 | 174.41 | 109 | 1.60 |

Table 3.4: Fit parameters for XMM-Int2 FFPs.

| Band vs Continuum | Model | Parameters | $\chi^2$ | DoF | $\chi^2_\nu$ |
|---|---|---|---|---|---|
| soft | linear | m = 2.09 ± 0.02<br>b = 0.02 ± 0.02 | 646.09 | 79 | 8.18 |
| | power-law | k = 2.105 ± 0.007<br>a = 0.98 ± 0.01 | 644.38 | 79 | 8.16 |
| | PLc | $\alpha$ = 3.7 ± 0.6<br>$\beta$ = 0.53 ± 0.09<br>c = −1.6± 0.6 | 616.56 | 78 | 7.90 |
| hard | linear | m = 0.171 ± 0.009<br>b = 0.091 ± 0.008 | 150.89 | 79 | 1.91 |
| | power-law | k = 0.264 ± 0.002<br>a = 0.62 ± 0.03 | 145.94 | 79 | 1.85 |
| | PLc | $\alpha$ = 173.103 ± 0.002<br>$\beta$ = 0.0009 ± 14.9392<br>c = −172.837 ± 0.002 | 141.56 | 78 | 1.81 |

Table 3.5: Fit parameters for XMM-Low2 FFPs.

| Band vs Continuum | Model | Parameters | $\chi^2$ | DoF | $\chi^2_\nu$ |
|---|---|---|---|---|---|
| soft | linear | m = 2.17 ± 0.03 <br> b = 0.026 ± 0.005 | 566.41 | 136 | 4.16 |
| | power-law | k = 2.21 ± 0.03 <br> a = 0.973 ± 0.009 | 583.06 | 136 | 4.29 |
| | PLc | $\alpha$ = 2.46 ± 0.05 <br> $\beta$ = 1.36 ± 0.04 <br> c = 0.16± 0.01 | 492.26 | 135 | 3.65 |
| hard | linear | m = 0.23 ± 0.01 <br> b = 0.106 ± 0.003 | 263.40 | 136 | 1.94 |
| | power-law | k = 0.29 ± 0.01 <br> a = 0.38 ± 0.02 | 255.51 | 136 | 1.88 |
| | PLc | $\alpha$ = 0.345 ± 0.002 <br> $\beta$ = 0.276 ± 0.004 <br> c = −0.063 ± 0.001 | 255.33 | 135 | 1.89 |

The fit parameters for each observation were compared to determine whether they were consistent between observations and whether the overall state of the source could be considered. Figure 3.22 plots the fit parameters of the linear and power-law fits for each observation.
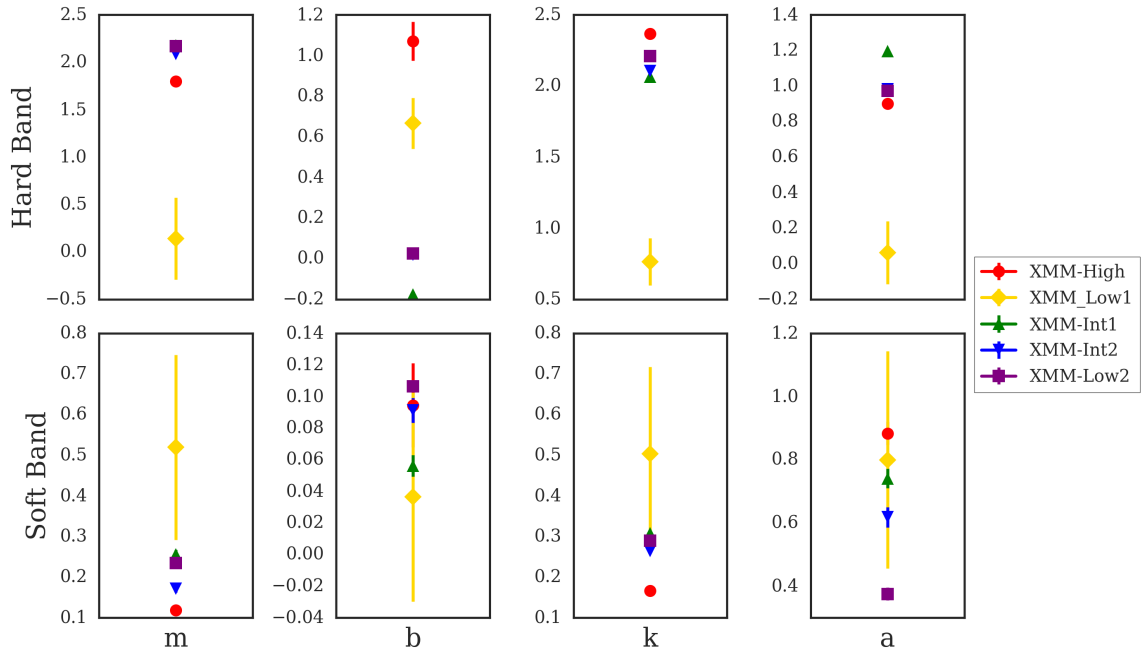


Figure 3.22: Comparison of parameters of linear (left two columns) and power-law (right two columns) fits for each observation. Parameters fit to soft band vs continuum FFPs are shown in top row while bottom row shows fit parameters for hard band vs continuum FFPs.

Since the fit parameters between the observations are not in agreement with one another, the epochs cannot be merged and so must be examined individually rather than analysing the overall state of Mrk 335. This indicates that different mechanisms are responsible for the variability in each epoch and so the epochs must be analysed separately.

## 3.4 TIME-RESOLVED FLUX-FLUX PLOTS

Flux-Flux Plots do not preserve timing information from the light curves, so in order to employ timing analysis, Time-Resolved Flux-Flux Plots were created (TRFFPs). These involve breaking the light curves up into sections and constructing a Flux-Flux Plot of each segment. Changes in fit goodness and parameters can indicate changing modes of variability during the course of an observation. The light curves were broken up into segments of ~20 ks (as shown in Figure 3.23), and fits made to each segment individually.
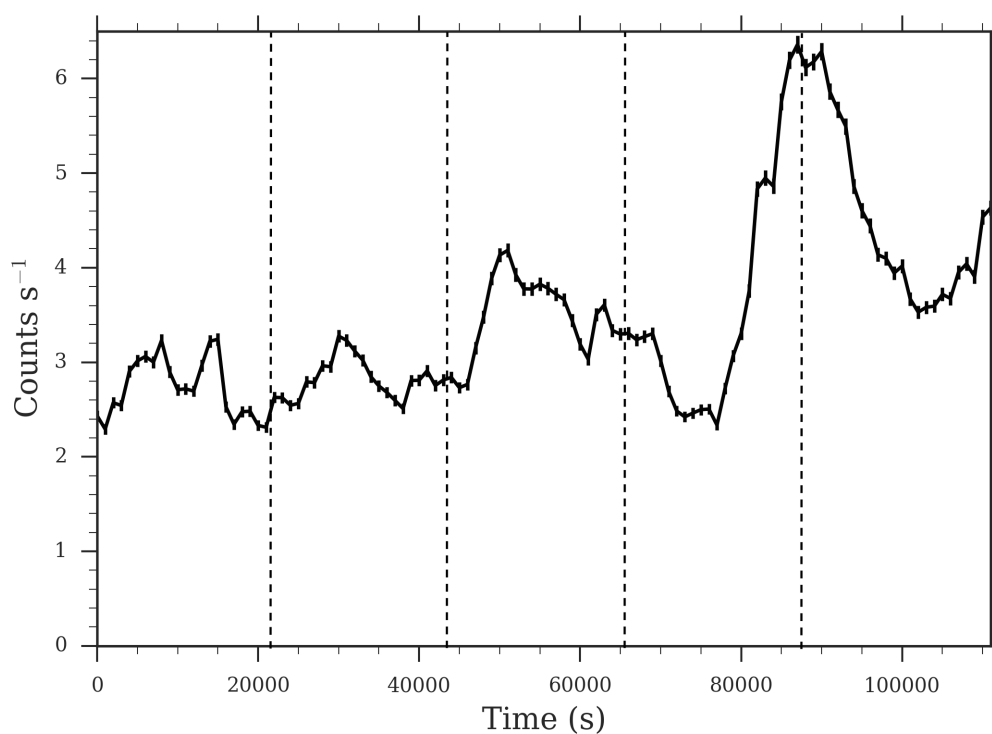


Figure 3.23: Broad-band (0.3 - 10 keV) light curve of XMM-Int1, showing segments used to construct TRFFPs.

This was done primarily to examine XMM-Int1 to determine if a single mode of variability is dominant throughout the observation, as that is the only observation

for which the residuals clearly differ between fits (see Figure 3.16). Soft band against

continuum TRFFPs for XMM-Int1 are shown in Figure 3.24. Residuals of the linear fit

to these plots are shown in Figure 3.25, while residuals of the power-law plus constant

fit are displayed in Figure 3.26. Table 3.6 displays parameters and goodness-of-fit

statistics for the fits to the Time-Resolved Flux-Flux Plots.
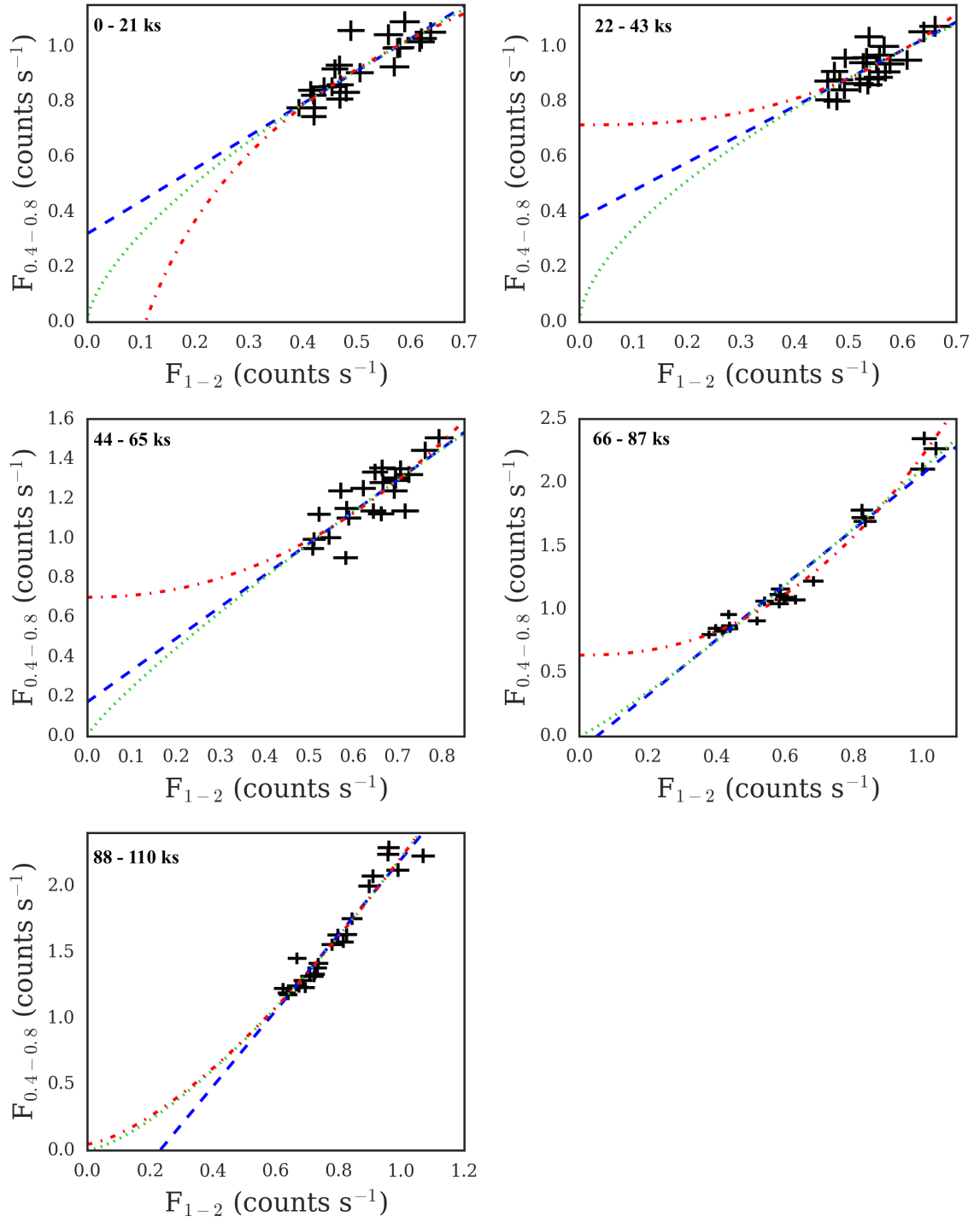
Figure 3.24: Time-Resolved Flux-Flux Plot of soft band vs continuum for XMM-Int1.
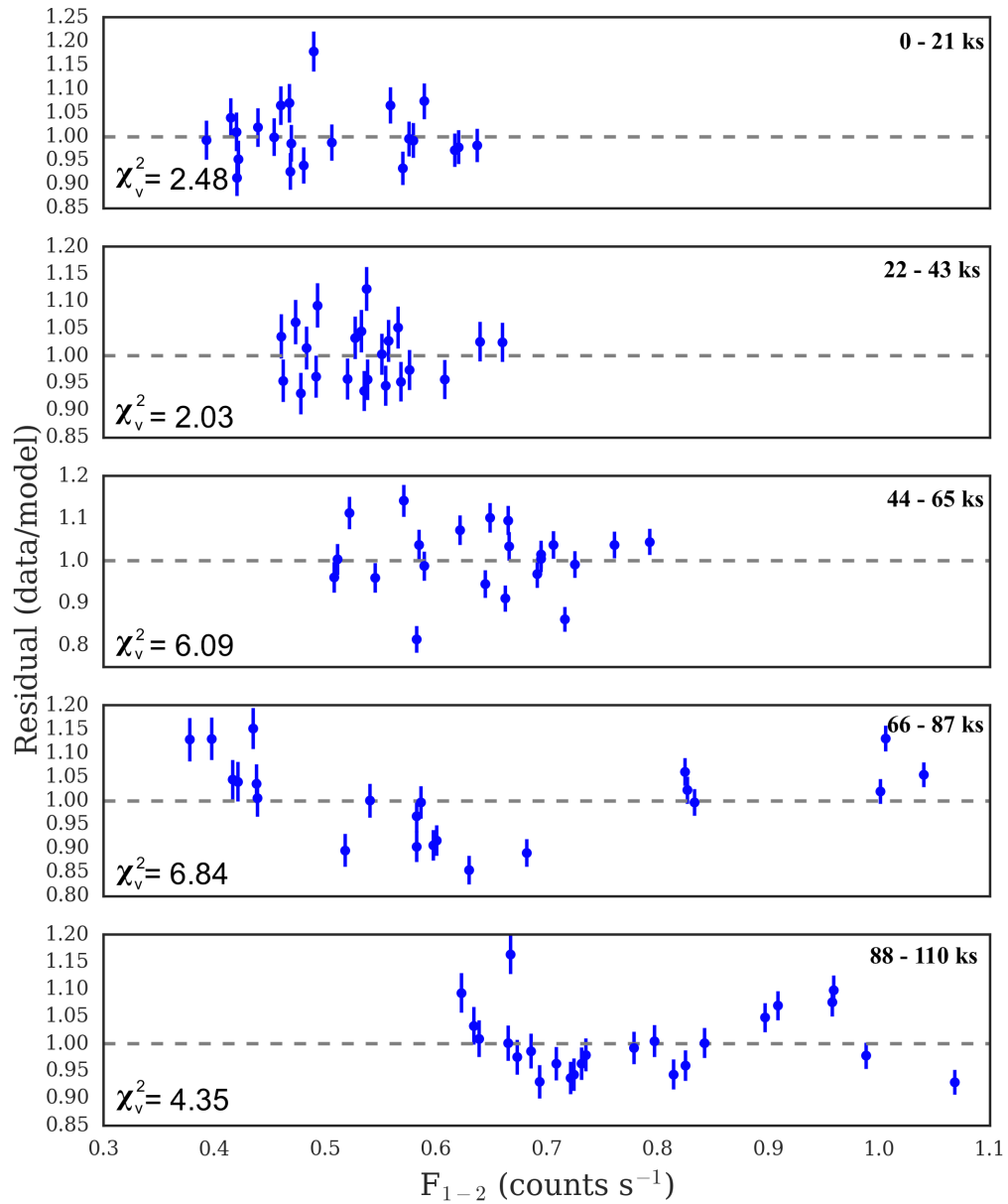
Figure 3.25: Residuals of linear fit to soft band vs continuum Time-Resolved Flux-Flux Plots of XMM-Int1.
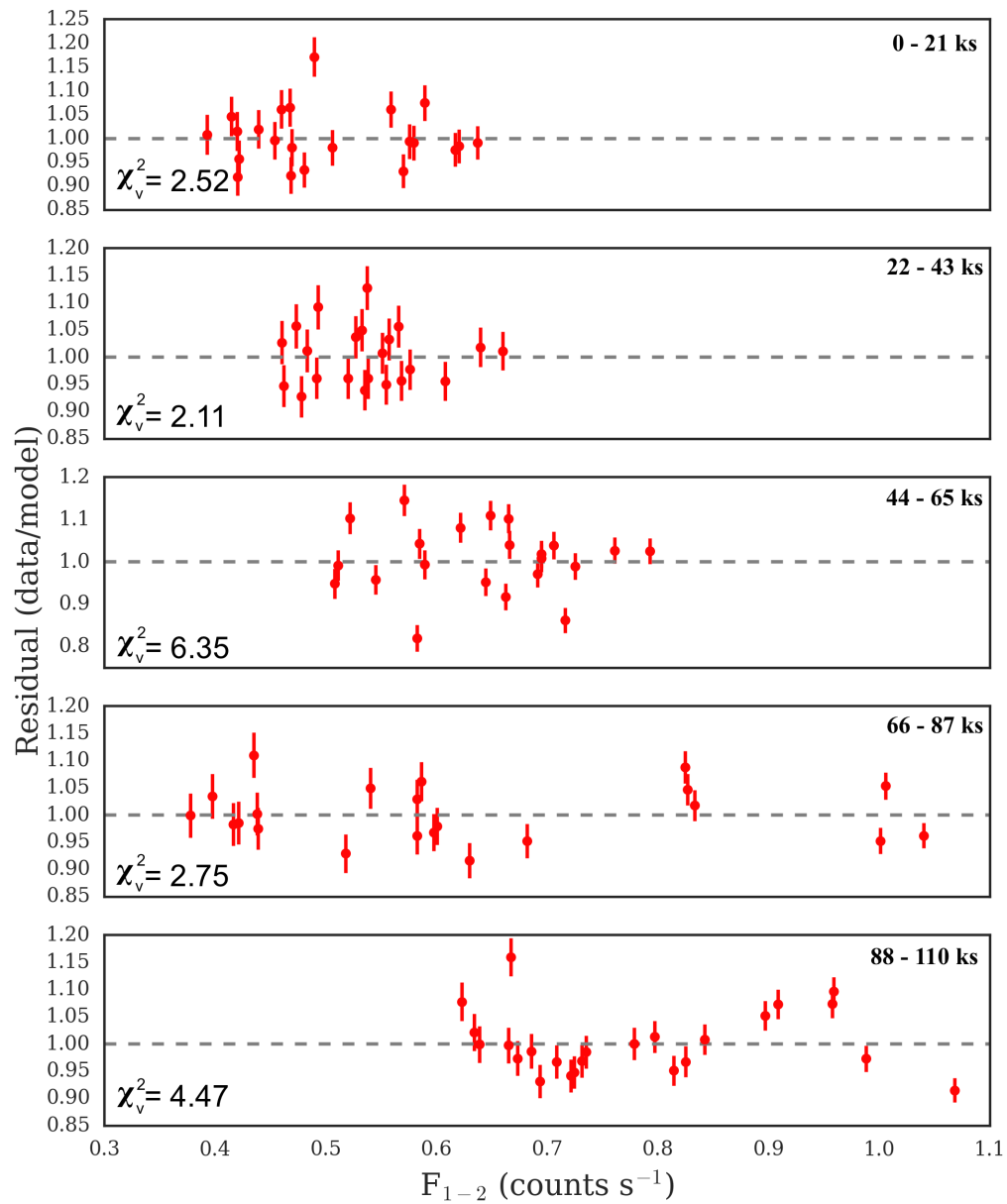
Figure 3.26: Residuals of power-law plus constant fit to soft band vs continuum Time-Resolved Flux-Flux Plots of XMM-Int1.

Table 3.6: Fit parameters for XMM-Int1 soft against continuum TRFFPs.

| Segment | Model | Parameters | $\chi^2$ | DoF | $\chi^2_\nu$ |
|---------|-------|-----------|----------|-----|--------------|
| 0 - 21 ks | linear | m = 1.2 ± 0.1 <br> b = 0.32 ± 0.05 | 49.56 | 20 | 2.48 |
| | power-law | k = 1.43 ± 0.05 <br> a = 0.65 ± 0.05 | 48.85 | 20 | 2.44 |
| | PLc | $\alpha$ = 102.076 ± 0.007 <br> $\beta$ = 0.006 ± 1.414 <br> c = −100.743 ± 0.007 | 47.86 | 19 | 2.52 |
| 22 - 43 ks | linear | m = 1.0 ± 0.1 <br> b = 0.37 ± 0.08 | 40.51 | 20 | 2.03 |
| | power-law | k = 1.34 ± 0.07 <br> a = 0.60 ± 0.08 | 40.72 | 20 | 2.04 |
| | PLc | $\alpha$ = 1.0 ± 0.5 <br> $\beta$ = 2.60 ± 2.33 <br> c = 1.0 ± 0.5 | 40.13 | 19 | 2.11 |
| 44 - 65 ks | linear | m = 1.6 ± 0.1 <br> b = 0.17 ± 0.07 | 121.78 | 20 | 6.09 |
| | power-law | k = 1.75 ± 0.05 <br> a = 0.86 ± 0.06 | 122.07 | 20 | 6.10 |
| | PLc | $\alpha$ = 1.26 ± 0.09 <br> $\beta$ = 2.13 ± 1.05 <br> c = 0.7 ± 0.2 | 120.73 | 19 | 6.35 |
| 66 - 87 ks | linear | m = 2.17 ± 0.05 <br> b = −0.11 ± 0.03 | 136.78 | 20 | 6.84 |
| | power-law | k = 2.10 ± 0.02 <br> a = 1.12 ± 0.02 | 123.09 | 20 | 6.15 |
| | PLc | $\alpha$ = 1.57 ± 0.04 <br> $\beta$ = 2.3 ± 0.2 <br> c = 0.64 ± 0.04 | 52.20 | 19 | 2.75 |
| 88 - 110 ks | linear | m = 2.87 ± 0.08 <br> b = −0.67 ± 0.06 | 95.74 | 22 | 4.35 |
| | power-law | k = 2.22 ± 0.02 <br> a = 1.41 ± 0.04 | 93.94 | 22 | 4.27 |
| | PLc | $\alpha$ = 2.2 ± 0.4 <br> $\beta$ = 1.5 ± 0.3 <br> c = 0.05 ± 0.36 | 93.92 | 21 | 4.47 |

## 3.5 MODELS

To investigate what varying parameters could produce the scatter in the Flux-Flux Plots seen here, a model of XMM-Int1 constructed by Gallo et al. (2013) was utilised. Time-resolved spectroscopy performed by Gallo et al. (2013) on XMM-Int1 found that for the first 70 ks of the observation, the photon index of the power-law as well as the normalisation of the reflection component were constant, after which they began to vary. Power-law normalisation was found to be variable during the entire observation.

The model of XMM-Int1 created by Gallo et al. (2013) was loaded into XSPEC and a script was implemented to vary the parameters of power-law photon index, power-law flux, and reflection flux in accordance with the trends of the parameters determined by Gallo et al. (2013). The flux from 0.4 - 0.8 keV and 1 - 2 keV was output after each variation, and this data used to construct a Flux-Flux Plot, shown in Figure 3.27.
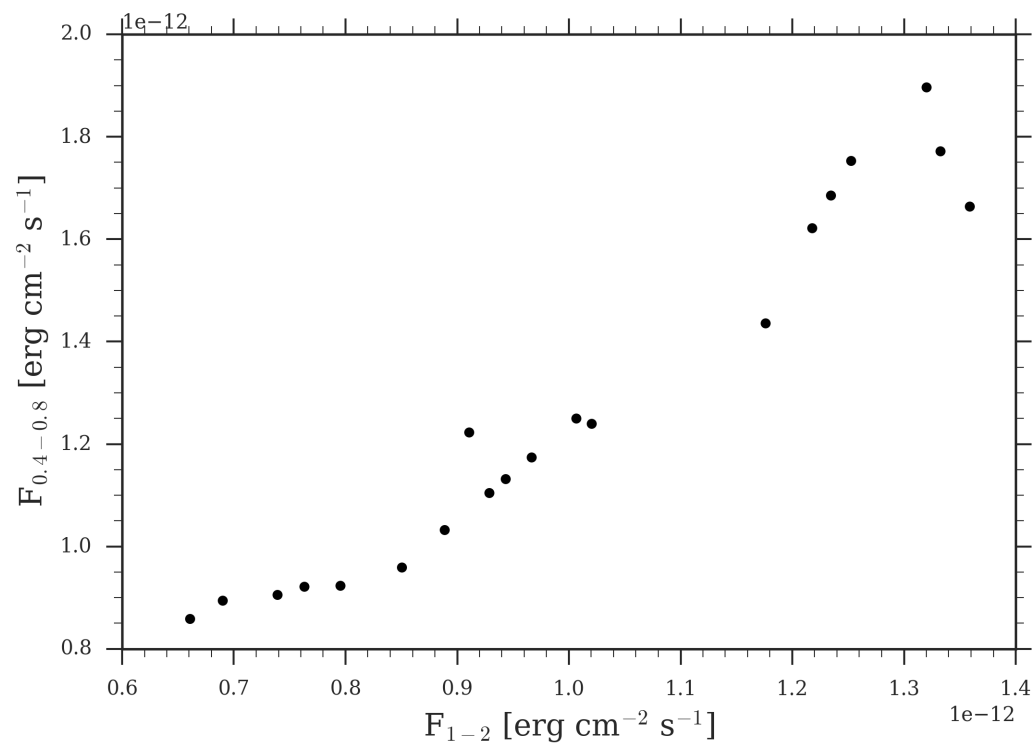
Figure 3.27: FFP constructed from varying three parameters (power-law photon index, power-law flux, reflection flux) of XMM-Int1 model constructed by Gallo et al. (2013).

# Chapter 4

# DISCUSSION

It was shown (Section 3.2.1) that the shape of the binned-up Flux-Flux Plots for Mrk 335 differ depending on the dimension the data are binned by. Tests revealed that binning dimension was indifferent to the variation of a single parameter, but the variation of multiple uncorrelated components produced a scattered FFP which was sensitive to binning dimensions. Because the FFPs for Mrk 335 *were* sensitive to binning dimensions, this indicates that the short-term variability observed in Mrk 335 is likely a result of multiple parameters changing simultaneously.

Examination of fits to individual epochs (Section 3.3) revealed that fit parameters did not agree between epochs (Figure 3.22). This prohibits the fitting of all epochs together and indicates that different modes of variability are in effect at different times. This has been observed previously in Mrk 335 (Gallo et al., 2013; Wilkins and Gallo, 2015a).

The fits of the linear, power-law and power-law plus constant models to each observation yielded poor fit statistics that were indistinguishable between the models. This indicates that the mode of variability of Mrk 335 cannot be described by a simple model. Models which result from the variation of only a single parameter are inadequate to represent the short-term variability that is seen in this object. It is likely then, that the variability exhibited by Mrk 335 results from a more complicated

system in which multiple components are varying simultaneously.

The residuals for the three models fit were identical for each observation, with the exception of XMM-Int1. It was for this reason that Time-Resolved Flux-Flux Plots were created for this observation, in order to investigate whether there was a time-dependence to the variability.

The Time-Resolved Flux-Flux Plots for XMM-Int1 reveal a change of fit in the fourth segment (66 - 87 ks). The previous three segments of the TRFFP show no distinction between the linear and power-law plus constant fit in the residuals (Figures 3.25 & 3.26), and the fit statistics were comparable between the two models. In the fourth segment, however, the power-law plus constant fit shows a significant improvement over the linear fit. This indicates that there is some change in the mode of variability around this time. The better fit statistics of the power-law plus constant model imply that the variability in this segment results from a change in the photon index with the presence of some constant spectral component (see Section 1.3).

This result is in agreement with spectral analysis of XMM-Int1 and XMM-Int2 performed by Gallo et al. (2013). Their time-resolved spectroscopy found that during XMM-Int1, the photon index of the power-law component was constant for the first 70 ks of the observation, after which it began to vary. The normalisation of the power-law was found to be variable for the duration of the observation. Both the photon index and normalisation of the power-law were found to vary for XMM-Int2. Additionally the normalisation of the reflection component was found to be constant for the first 70 ks of XMM-Int1, variable for the remainder of the observation, and variable for XMM-Int2. These model-dependent results are consistent with the model-

independent analysis yielded by the TRFFPs.

Analysis of the light curve of XMM-Int1 (Figure 3.23) shows that a flare in the light curve begins at ∼70 ks, which is when the TRFFPs reveal the change in variability mode. This indicates that this changing mode of variability could be related to events occurring in the light curve.

The FFP constructed by varying three parameters of the XMM-Int1 model created by Gallo et al. (2013) (Figure 3.27) closely resembles the trend seen in the actual data (Figure 3.16). This indicates that the variability exhibited during this epoch may be due to variations of these parameters (power-law photon index, power-law flux, reflection flux) in the manner determined by Gallo et al. (2013).

# Chapter 5

# Conclusions

The model-independent method of Flux-Flux Plots was employed to investigate the nature of short-term spectral variability in the X-ray spectrum of Markarian 335. Light curves in two energy bands were plotted against one another and simple physical models fit to the data to determine whether they could account for the spectral variability observed.

Energy bands used to construct Flux-Flux Plots were chosen by fitting spectra with an absorbed power-law and identifying the continuum, soft excess and hard excess.

The Flux-Flux Plots were binned-up and the results were found to be sensitive to the primary axis the data was binned by. Tests found that binning dimension had no effect on models in which only one parameter was varying, but was significant in tests where more than one parameter was varying. Because the Flux-Flux Plots of Mrk 335 *are* sensitive to binning dimension, it was determined that there are multiple varying parameters contributing to the spectral variability in this AGN.

For the analysis, the data were not binned up after constructing the Flux-Flux Plots due to the conflicting results from selected binning dimension. The light curves were binned in time by 1 ks, chosen to optimise signal-to-noise ratio while maintaining timing resolution.

Linear, power-law and power-law plus constant fits were made to the Flux-Flux Plots and found to be poor fits to the data. The three fits were also indistinguishable from one another (with the exception of XMM-Int1), yielding comparable fit statistics and identical residuals. This indicates that the mode of variability in Mrk 335 cannot be described by a simple model with only one varying parameter.

It was found that for the observation XMM-Int1, the power-law plus constant fit was significantly better than the linear and power-law fits. This was the only observation for which the fits were distinguishable. To investigate whether this fit improvement was time-dependent, Time-Resolved Flux-Flux Plots were created, for which the observation was broken up into five segments of $\sim$ 20 ks each. Flux-Flux Plots were made for each segment and the three simple models fit to each plot. It was found that in the 66 - 87 ks segment the power-law plus constant fit becomes significantly better, indicating that there is some change in the mode of variability around this time. This is in agreement with results from time-resolved spectroscopy performed by Gallo et al. (2013). Additionally, this segment of the TRFPP corresponds to a flare in the light curve that begins at $\sim$ 70 ks, indicating that the change of variability could be related to events occurring in the light curve.

Varying multiple parameter of a model of XMM-Int1 yielded a Flux-Flux Plot that simple fits could not accurately represent. The scatter exhibited by this plot resembled that seen in the observational data.

The short-term spectral variability exhibited by Markarian 335 cannot be adequately described by simple models in which only one parameter is varying. It is likely that the variability results from a more complicated model with multiple pa-

rameters varying independently.

# Bibliography

B.W. Carrol and D.A. Ostlie. *An Introduction to Modern Astrophysics*. Pearson Education Inc., Addison-Wesley, San Francisco, second edition, 2007.

C. Done, S. W. Davis, C. Jin, O. Blaes, and M. Ward. Intrinsic disc emission and the soft X-ray excess in active galactic nuclei. *MNRAS*, 420:1848, 2012.

A.A. Galeev, R. Rosner, and G.S. Vaiana. Structured coronae of accretion disks. *The Astrophysical Journal*, 229:318–326, 1979.

L. C. Gallo, A. C. Fabian, D. Grupe, K. Bonson, S. Komossa, A. L. Longinotto, G. Miniutti, D. J. Walton, A. Zoghbi, and S. Mathur. A blurred reflection interpretation for the intermediate flux state in Mrk 335. *MNRAS*, 428:1191–1200, 2013.

L.C. Gallo. Revealing the Innermost Regions of Active Galaxies. *JRASC*, 749: 143–150, 2011.

M. Gierliński and C. Done. Energy-dependent variability and the origin of the soft X-ray excess in active galactic nuclei. *MNRAS*, 371:L16–L20, 2006.

A.G. Gonzalez, D.R. Wilkins, and L.C. Gallo. Exploring various corona geometries and their emissivity profiles. *MNRAS*, in print.

C.J. Grier, B.M. Peterson, R.W. Pogge, K.D. Denney, M.C. Bentz, P. Martini, S.G. Sergeev, S. Kaspi, Y. Zu, C.S. Kochanek, B.J. Shappee, K.Z. Stanek, C. Araya Salvo, T.G. Beatty, J.C. Bird, D.J. Bord, G.A. Borman, X. Che, C. Chen, S.A. Cohen, M. Dietrich, V.T. Doroshenko, Y.S. Efimov, N. Free, I. Ginsburg, C.B. Henderson, K. Horne, A.L. King, K. Mogren, M. Molina, A.M. Mosquera, S.V. Nazarov, D.N. Okhmat, O. Pejcha, S. Rafter, J.C. Shields, J. Skowron, D.M. Szczygiel, M. Valluri, and J.L. van Saders. A Reverberation Lag for the High-ionization Component of the Broad-line Region in the Narrow-line Seyfert 1 Mrk 335. *The Astrophysical Journal*, 744:L4, 2012.

D. Grupe, S. Komossa, and L.C. Gallo. Discovery of the narrow-line Seyfert 1 galaxy Markarian 335 in a historical low X-ray flux state. *The Astrophysical Journal*, 668: L111, 2007.

F. Jansen, D. Lumb, B. Altieri, J. Clavel, M. Ehle, C. Erd, C. Gabriel, M. Guainazzi, P. Gondoin, R. Much, R. Munoz, M. Santos, N. Schartel, D. Texier, and G. Vacanti. XMM-Newton observatory. *Astronomy & Astrophysics*, 365:L1–L6, 2001.

P.M.W. Kalberla, W.B. Burton, Dap Hartmann, E.M. Arnal, E. Bajaja, R. Morras, and W.G.L. Pöppel. The Leiden/Argentine/Bonn (LAB) Survey of Galactic HI. Final data release of the combined LDS and IAR surveys with improved stray-radiation corrections. *Astronomy & Astrophysics*, 440:775, 2005.

E.S. Kammoun, I.E. Papadakis, and B.M. Sabra. Variability of the Soft X-ray Excess in IRAS 13224-3809. *Astronomy & Astrophysics*, 582:A40, 2015.

G. Ponti, G. Miniutti, M. Cappi, L. Maraschi, A.C. Fabian, and K. Iwasawa. XMM-Newton study of the complex and variable spectrum of NGC 4051. *MNRAS*, 368: 903–916, 2006.

R.R. Ross and A.C. Fabian. A comprehensive range of X-ray ionized-reflection models. *MNRAS*, 358:211, 2005.

Barbara Ryden and Bradley M. Peterson. *Foundation of Astrophysics*. Pearson Education Inc., Addison-Wesley, San Francisco, 2010.

L. Strüder, U. Briel, K. Dennerl, R. Hartmann, E. Kendziorra, N. Meidinger, E. Pfeffermann, C. Reppin, B. Aschenbach, W. Bornemann, H. Bräuninger, W. Burkert, M. Elender, M. Freyberg, F. Haberl, G. Hartner, F. Heuschmann, H. Hippmann, E. Kastelic, S. Kemmer, G. Kettenring, W. Kink, N. Krause, S. Müller, A. Oppitz, W. Pietsch, M. Popp, P. Predehl, A. Read, K. H. Stephan, D. Stötter, J. Trümper, P. Holl, J. Kemmer, H. Soltau, R. Stötter, U. Weber, U. Weichert, C. von Zanthier, D. Carathanassis, G. Lutz, R. H. Richter, P. Solc, H. Böttcher, M. Kuster, R. Staubert, A. Abbey, A. Holland, M. Turner, M. Balasini, G. F. Bignami, N. La Palombara, G. Villa, W. Buttler, F. Gianini, R. Lainé, D. Lumb, and P. Dhez. The European Photon Imaging Camera on XMM-Newton: The pn-CCD camera. *Astronomy & Astrophysics*, 365:L18–L26, 2001.

R.D. Taylor, P. Uttley, and I.M. McHardy. The nature of X-ray spectral variability in Seyfert galaxies. *MNRAS*, 342:L31–L35, 2003.

P. Uttley, R.D. Taylor, I.M. McHardy, M.J. Page, K.O. Mason, G. Lamer, and A. Fruscione. Complex X-ray spectral behaviour of NGC 4051 in the low flux state. *MNRAS*, 347:1345–1356, 2004.

D.R. Wilkins. Driving Extreme Variability: Measuring the evolving coronae and evidence for jet launching in AGN. *Astron. Nachr.*, 337(4-5), 2016.

D.R. Wilkins and L.C. Gallo. Driving extreme variability: the evolving corona and evidence for jet launching in Markarian 335. *MNRAS*, 449:129–146, 2015a.

D.R. Wilkins and L.C. Gallo. The Comptonisation of accretion disc X-ray emission: Consequences for X-ray reflection and the geometry of AGN coronae. *MNRAS*, 448: 703, 2015b.

E. Zackrisson. *Quasars and Low Surface Brightness Galaxies as Probes of Dark Matter*. PhD thesis, Stockholm University, 2005.